JOURNAL OF GEOPHYSICAL RESEARCH, VOL. 111, B12S07, doi:10.1029/2006JB004514, 2006

Characterizing the superparamagnetic grain distribution $f(V, H_k)$ by thermal fluctuation tomography

Mike Jackson,[1] Brian Carter-Stiglitz,[1] Ramon Egli,[1] and Peter Solheid[1]

Received 18 May 2006; revised 31 August 2006; accepted 25 September 2006; published 28 November 2006.

[1] In 1965, D. J. Dunlop showed that the joint distribution of particle volumes and microcoercivities $f(V, H_{k0})$ can be determined for magnetically monomineralic, thermally stable single-domain (SSD) ensembles by taking advantage of the joint temperature and field dependence of relaxation time. We have developed a procedure that follows Dunlop's strategy to obtain $f(V, H_{k0})$ for ensembles containing both superparamagnetic and SSD grains, based on backfield remanence curves measured over a range of temperatures. Each point on the derivative curves represents the integrated contribution from grains that lie along a corresponding blocking contour on the Néel plot. A suitable set of such line integral samples can be used to reconstruct the $f(V, H_{k0})$ distribution using the methods of tomographic imaging. Samples of the basal Tiva Canyon Tuff have narrow size distributions of elongate Ti-poor titanomagnetite. Tomographic inversion of the low-temperature backfield spectra yield sharply peaked $f(V, H_{k0})$ distributions, from which we calculate modal grain dimensions in good agreement with those observed by transmission electron microscopy. Analysis of synthetic samples containing bimodal populations clearly distinguishes the two modes. Because our simplified forward calculations incompletely account for the effects of orientation distribution, the width of the coercivity distribution at each temperature is underestimated, and consequently, the inverse calculations yield grain distributions that are overly broad. Frequency- and temperature-dependent susceptibilities calculated for the inverted $f(V, H_{k0})$ distributions accord fairly well with measured susceptibilities for the weakly interacting Tiva Canyon samples, less well for a moderately interacting paleosol specimen, and poorly for a strongly interacting ferrofluid.

Citation: Jackson, M., B. Carter-Stiglitz, R. Egli, and P. Solheid (2006), Characterizing the superparamagnetic grain distribution $f(V, H_k)$ by thermal fluctuation tomography, *J. Geophys. Res.*, *111*, B12S07, doi:10.1029/2006JB004514.

1. Introduction

[2] *Dunlop* [1965, p. 459] wrote that "the ultimate aim of theoretical rock magnetism is to be able to predict the magnetic behavior of any rock sample." Magnetic behavior (i.e., the response of remanent and induced magnetizations to experimental variables including applied field, temperature and time) depends on magnetic mineralogy, on the distribution of grain sizes (domain states) and shapes, and on the magnetostatic interactions among particles. At present, a comprehensive quantitative theory exists only for populations of noninteracting single-domain (SD) grains that reverse by coherent rotation of spins [*Stoner and Wohlfarth*, 1948; *Néel*, 1949; *Brown*, 1959; *Dunlop and West*, 1969]; a comparably complete predictive theory for multidomain (MD) grain populations remains to be developed. Given a theory such as that of *Néel* [1949] and complete knowledge of the magnetic grain characteristics, we can predict magnetic behavior quantitatively and accurately for a population of ideal SD particles. Conversely, detailed characterization of magnetic behavior can be combined with Néel theory to quantify the unknown distribution of magnetic grain sizes and shapes in a sample containing SD particles, including thermally stable SD (SSD) and superparamagnetic (SP) grains.

[3] Accurate prediction of magnetic behavior under various natural and laboratory conditions is the keystone for a wide range of paleomagnetic applications including paleointensity [*Perrin*, 1998; *Dunlop and Özdemir*, 2000; *Fabian*, 2001; *Carlut and Kent*, 2002; *Yu and Dunlop*, 2003; *Coe et al.*, 2004; *Carvallo et al.*, 2005; *Dunlop et al.*, 2005; *Yu and Tauxe*, 2005] and paleothermometry [*Dunlop et al.*, 1997a, 1997b]. Such applications depend critically on magnetic mineralogy and grain attributes, and therefore detailed rock magnetic characterization is an integral part of these studies. Moreover, a detailed inventory of magnetic grain sizes and shapes often contains significant information about sediment transport, depositional conditions, and geochemical environments; therefore magnetic characterization has become a significant tool in paleoenvironmental

[1]Institute for Rock Magnetism, Department of Geology and Geophysics, University of Minnesota, Minneapolis, Minnesota, USA.

0148-0227/06/2006JB004514$09.00

Table 1. Notation and Definitions

Symbol	Property	Definition
H_K	microscopic coercivity or anisotropy field	critical field (parallel to grain long axis) for moment reversal in the absence of thermal fluctuations
$H_{SW}(\varphi)$	Stoner-Wohlfarth switching field	critical field (at a specified angle φ to grain long axis) for moment reversal in the absence of thermal fluctuations: $0.5 \leq H_{SW}/H_K \leq 1.0$
H_q	thermal fluctuation field	amount by which thermal fluctuations decrease the critical field for moment reversal
H_B	(un)blocking field	critical field (at a specified angle to grain long axis) for moment reversal in the presence of thermal fluctuations: $H_B = H_{SW} - H_q$
H_{CR}	coercivity of remanence	field axis intercept (absolute value) of the remanent hysteresis curve (experimentally determined): $H_{CR} \sim H_B \leq H_{SW} \leq H_K$
H_{app}	DC field	applied DC field during a particular experiment. In the case of DC demagnetization curves, H_{app} is the backfield applied just prior to magnetization measurement
H_0	maximum AC field	maximum field applied during the measurement of AC susceptibility
T_0	reference temperature	used in defining temperature dependence of saturation magnetization, often taken as room temperature (~300 K); in this paper taken as 0 K

research [*Thompson and Oldfield*, 1986; *Heller and Evans*, 1995; *Verosub and Roberts*, 1995; *Dekkers*, 1997; *Maher and Thompson*, 1999; *Dunlop*, 2002].

[4] Although simple scalar properties such as bulk susceptibility may have paleoenvironmental significance [*Heller et al.*, 1993; *Maher et al.*, 1994; *Maher and Thompson*, 1995], in most cases it is far more informative to look at spectral properties such as the coercivity distribution [*Dunlop*, 1972, 1986; *Robertson and France*, 1994; *Heslop et al.*, 2002; *Egli*, 2003, 2004a, 2004b]. Preisach analysis and its descendant FORC analysis go a step further by mapping out a distribution of "hysteron" properties H_c and H_u which are interpreted as coercivity and interaction field, respectively [*Roberts et al.*, 2000; *Pike et al.*, 2001; *Newell*, 2005]. FORC distributions are purported to have some predictive value concerning behavior during Thellier-Thellier paleointensity experiments [*Carvallo et al.*, 2005], but such predictions are at present qualitative in nature.

[5] In Néel theory the grain volume is a key variable, and various studies have used this as the basis for transforming the distribution of unblocking temperatures into a volume distribution [e.g., *Worm et al.*, 1988; *Worm and Jackson*, 1999]. This requires us to make the assumption that the distribution of coercivities is much narrower than that of grain size (as pointed out by *Dunlop* [1965]), since the unblocking temperature (the SSD-SP transition in zero field) depends on the product of grain volume and coercivity (see section 2 for details). Similarly *Shcherbakov and Fabian* [2005] have shown that temperature- and frequency-dependent low-field susceptibilities can be mapped into a volume distribution only when some relationship between grain volume and coercivity is specified a priori.

[6] *Dunlop* [1965] showed that in contrast to these weak field thermomagnetic granulometry methods, it is possible to combine field- and temperature-dependent measurements to determine unambiguously the joint distribution of grain volumes and microcoercivities, without prior specification of any relation between these two properties or their individual distributions. There is still one relationship that we must assume, however, namely, the temperature dependence of microcoercivity. This is governed by the dominant anisotropy mechanism, which may involve control by grain shape, stress or crystallography. In this paper we will follow *Dunlop* [1965] in focusing on shape anisotropy, which typically dominates for soft, intense ferrimagnets such as magnetite. If we further assume that the magnetic grain shapes are ellipsoids of revolution, we can directly translate microcoercivities into aspect ratios and vice versa.

[7] The two-dimensional joint distribution of grain size and microcoercivity can be represented by density contours on a "Néel plot" with axes V and H_{k0} [*Néel*, 1949; *Dunlop*, 1965]. (Variables and notation are summarized in Table 1). Microcoercivity varies with temperature; H_{k0} is defined in this paper as the microcoercivity at 0 K, which (assuming dominant shape anisotropy) depends only on mineralogy and aspect ratio. V and H_{k0} are therefore uniquely defined for each individual grain. *Néel* [1949] used such plots for diagrammatic representation of magnetization/demagnetization processes for SD grain populations, in which V and H_{k0} are centrally important in determining magnetic stability under different applied fields and temperatures.

2. Theory

2.1. Shape Anisotropy and Microscopic Coercivity H_K

[8] In the absence of thermal fluctuations, the hysteresis of shape-dominated SD grain populations can be modeled according to the theory of *Stoner and Wohlfarth* [1948]. We consider each grain to be a uniaxial prolate ellipsoid with demagnetizing factors N_a and N_b in the polar and equatorial directions, respectively. We also assume that grains remain uniformly magnetized in applied fields of any strength and orientation, and thus that they reverse by coherent rotation. The critical field required to reverse the magnetization of such a grain depends on its shape (aspect ratio a/b), its magnetization intensity, and its orientation with respect to the applied field. For a single grain aligned with the externally applied field (or for a population of identical noninteracting aligned grains), the hysteresis loop is square, with the moment(s) switching at fields equal to $\pm H_K$, the microscopic coercivity:

$$H_K = (N_b - N_a)M_S = \Delta N M_S, \quad (1)$$

where M_S is the volumetric saturation magnetization of the ferrimagnetic material (e.g., 480 kA/m for magnetite).

[9] When a field is applied at an arbitrary angle φ to the long axis of the grain(s), the critical field for moment reversal (the switching field, $H_{SW}(\varphi)$) is generally less than H_K, ranging from a minimum of $H_K/2$ for an angle of 45°, to the maximum value of H_K for a field applied parallel or perpendicular to the long axes [*Stoner and Wohlfarth*, 1948; see also *Dunlop and Özdemir*, 1997, section 8.3]. Thus, as defined here, $H_K = H_{SW}(0)$ is determined solely by grain shape (ΔN) and mineralogy (M_S), whereas H_{SW} depends on these two factors and also on grain orientation with respect to the applied field.

[10] Although thermal fluctuations are not explicitly considered in these definitions, H_K and H_{SW} depend on temperature through their proportionality with M_S:

$$\beta(T) = M_S(T)/M_{S0} = H_K(T)/H_{K0}, \tag{2}$$

where the subscript 0 denotes the value at a reference temperature T_0, often taken as 300 K; in this paper we define $T_0 = 0$ K. (The second equality in (2) only holds for shape anisotropy). A common analytical approximation is

$$\beta(T) = \left[\frac{T_C - T}{T_C - T_0}\right]^{\gamma} \tag{3}$$

with $\gamma \sim 0.5$. For magnetite $\gamma = 0.43$ is commonly used above room temperature [*Dunlop and Özdemir*, 1997, section 2.5]. Below room temperature the variation in M_S is weaker, and can be described by Bloch's "$T^{3/2}$ law" [e.g., *Worm and Jackson*, 1999] or by a lower value of γ.

2.2. Remanent Coercivity H_{CR}

[11] For real samples, there is always a distribution of grain shapes and orientations, and consequently there is a distribution of switching fields $f(H_{SW})$. The remanent coercivity H_{CR}, the field axis intercept of the remanent hysteresis loop, represents a weighted average or expected value of this distribution, in the absence of thermal fluctuations. For randomly oriented identical particles, Stoner-Wohlfarth theory predicts

$$H_{CR} = \langle f(H_{SW})\rangle = 0.524 H_K, \tag{4}$$

where the angle brackets denote (weighted) averaging. H_K is in general not directly measurable, but an expected value can be obtained by this equation from a measured H_{CR}.

[12] The coercivity distribution [*Dunlop*, 1972, 1986; *Robertson and France*, 1994; *Heslop et al.*, 2002; *Egli*, 2003, 2004a, 2004b] is typically quantified by calculating the derivative (with respect to applied field) of a magnetization or demagnetization curve including isothermal remanent magnetization (IRM) acquisition; DC demagnetization of IRM (the backfield remanence curve); and AF demagnetization of IRM. In the absence of interactions, each of these yields the same coercivity spectrum for a given SD population [*Dunlop and Özdemir*, 1997]. The coercivity spectrum thus obtained is closely related to (but not necessarily identical to) the distribution of H_{SW}.

2.3. Thermal Fluctuation Field H_q

[13] Differences between the experimentally defined H_{CR} and the theoretically defined $\langle f(H_{SW})\rangle$ in noninteracting nanoparticle populations are primarily due to the effects of thermal fluctuations, for which the theory was developed by *Néel* [1949] and elaborated by *Brown* [1959, 1963]. Random thermal fluctuations sporadically add to the applied field energy in driving magnetic moments over the energy barrier for reversal, and thus in effect they act as an additional applied field, which Néel called the thermal fluctuation field H_q.

[14] The relaxation time for an aligned population of identical grains with volume V, in an applied field $H_{app} \leq H_K$ parallel to the grain long axes, is

$$\tau = \tau_0 \exp\left(\frac{\mu_0 V M_S H_K \left(1 - |H_{app}|/H_K\right)^{\alpha}}{2kT}\right), \tag{5}$$

where $\tau_0 \sim 10^{-9}$–10^{-10} s, $\mu_0 = 4\pi \times 10^{-7}$ H/m, $k = 1.38 \times 10^{-23}$ J/K, and α depends on the relative orientations of field and easy axes; for the parallel case treated by Néel, $\alpha = 2$. As the applied field strength approaches H_K, the relaxation time drops sharply and the magnetization quickly equilibrates. Following Néel, we can define the blocking field as that which reduces τ to a value equal to the measurement time constant τ_m:

$$\begin{aligned} H_B &= H_K - \left(\frac{2kTH_K \ln(\tau_m/\tau_0)}{\mu_0 V M_S}\right)^{1/2} \\ &= H_K - \left(\frac{2kT\Delta N \ln(\tau_m/\tau_0)}{\mu_0 V}\right)^{1/2} = H_K - H_q, \end{aligned} \tag{6}$$

obtained by setting $\tau = \tau_m$ in (5) and solving for $H_{app} = H_B$. Note that H_q is proportional to $T^{1/2}$ and to $V^{-1/2}$, so it is most important for small grains and/or high temperatures.

[15] For a randomly oriented population of identical grains, the derivation is considerably more complicated, but *Egli and Lowrie* [2002] have obtained an expression equivalent to

$$\begin{aligned} H_q = 0.801 &\left(\frac{kT\sqrt{H_K}}{\mu_0 V M_S}\right)^{2/3} \ln^{2/3} \\ &\cdot \left[\frac{1}{3.8\tau_0 f_{AC}\mu_0 \Delta\tilde{H}\sqrt{\mu_0 H_K}}\left(\frac{kT}{VM_S}\right)^{3/2}\right] \end{aligned} \tag{7}$$

for the case of alternating fields with frequency f_{AC} and half cycle decrement $\Delta\tilde{H}$. Here we modify this for DC fields:

$$H_q = 0.801\left(\frac{kT\sqrt{H_K}}{\mu_0 V M_S}\right)^{2/3} \ln^{2/3}\left[\frac{\tau_{\exp}}{\tau_0 \mu_0 \Delta H_{DC}}\left(\frac{kT}{VM_S}\right)^{3/2}\right], \tag{8}$$

where the exposure time $\tau_{\exp}$ for the backfield treatments is approximately 1 sec, and ΔH_{DC} is the difference between successive backfields. A log-log plot of the tabulated values from *Egli and Lowrie* [2002] (not shown) indicates that to a

fairly good approximation, H_q is in this case proportional to $T^{3/4}$ and to $V^{-3/4}$, so the thermal fluctuation field changes more rapidly with temperature and with grain size for a randomly oriented population than for an aligned one.

[16] In general, for a sample containing identical SD grains we have the following relations: $H_B(T) \leq \langle f(H_{SW}(T))\rangle \leq H_K(T) = \Delta N M_S(T)$. The first inequality is due to thermal fluctuations (in whose absence H_{CR} can be equated with the Stoner-Wohlfarth mean switching field) and the second inequality is determined by the orientation distribution.

2.4. Thermal Fluctuation Analysis

[17] *Dunlop* [1976] assumed dominant shape anisotropy (equation (2)), took $H_{CR}(T) \sim H_B(T)$ and rearranged (6) to obtain

$$\frac{H_{CR}(T)}{\beta(T)} = H_{K0} - \left(\frac{2kH_{K0}\ln(\tau_m/\tau_0)}{\mu_0 V M_{S0}}\right)^{1/2} \frac{T^{1/2}}{\beta(T)}. \quad (9)$$

Thus for an aligned population of identical grains, a plot of measured $H_{CR}(T)$ against $T^{1/2}$ (each scaled by measured or assumed values of $1/\beta(T)$) should yield a straight line, with an intercept of H_{K0} and a (negative) slope from which grain volume may be calculated, assuming M_{S0} is known. For samples with known narrow unimodal distributions of grain size and shape, *Dunlop* [1976] found that (9) gives reasonable estimates of the mean values $\langle V\rangle$ and $\langle H_{K0}\rangle$. In this article we will compare the results of thermal fluctuation analysis to those produced by our thermal fluctuation tomography technique. The two techniques are closely related and a comparison of the two is pedagogically useful.

[18] Equation (9) properly applies to aligned particles and a parallel applied field. For the randomly oriented case it would be appropriate to begin with equation (8), but (8) is not easily linearized. We start with equation (5) and follow *Dunlop*'s [1976] derivation with two modifications: we take $\alpha = 3/2$ [*Victora*, 1989; see also *Walton*, 1990], and replace H_{K0} in the field-dependent term with $H_{CR0} = \langle f(H_{SW})\rangle_0 = 0.524\ H_{K0}$. We obtain the following approximation for the randomly oriented population:

$$\frac{H_{CR}(T)}{\beta(T)} = H_{SW0} - H_{SW0}\left(\frac{2k\ln(\tau_m/\tau_0)}{\mu_0 V M_{S0} H_{K0}}\right)^{1/\alpha} \frac{T^{1/\alpha}}{[\beta(T)]^{2/\alpha}}, \quad (10)$$

where $H_{SW0} = 0.524 H_{K0}$.

2.5. Grain Distribution $f(V, H_{K0})$

[19] For broad or polymodal distributions of grain size and shape, thermal fluctuation analysis may be expected to yield nonlinear plots of $H_{CR}(T)$ against $T^{1/2}$, with slopes and intercepts that may not have a simple relationship to modal grain dimensions. A more general approach developed by *Dunlop* [1965] [see also *Dunlop and West*, 1969; *Dunlop and Özdemir*, 1997, section 8.12] allows us to map out $f(V, H_{K0})$, i.e., the detailed two-dimensional distribution of grain volumes and microcoercivities/shapes.

[20] Dunlop's approach is based on repeated steps of selective magnetization and stepwise demagnetization. For an aligned population of nonidentical grains, the unique blocking contour for each experimental condition (T, H_{app}, τ_m) is the set of (V, H_{K0}) for which $\tau(T, H_{app}, V, H_{K0}) = \tau_m$ (equation (5)), or equivalently, for which $H_B(T, V, H_{K0}, \tau_m) = H_{app}$ (equation (6)). A weak field pTRM given over the temperature interval (T_1, T_2), where $T_1 > T_2$, selectively magnetizes grains with (V, H_{K0}) lying between the weak field blocking contours for those temperatures (Figure 1a). Subsequent stepwise AF demagnetization progressively erases the pTRM, and the loss at each step can be equated with the remanence contribution from grains lying in a small, well-defined quadrilateral region of the Néel plot, bounded by the room temperature blocking contours for $\tilde{H}_1$ and $\tilde{H}_2$, and the weak field blocking contours for T_1 and T_2 (Figure 1). Repeating the process for pTRMs imprinted over different temperature intervals thus allows mapping out of the entire grain distribution [*Dunlop*, 1965].

2.6. Thermal Fluctuation Tomography

[21] Dunlop's approach is not readily extended to the finest grain populations that are superparamagnetic at room temperature, because presently available commercial instrumentation does not allow the necessary AF demagnetization and measurement cycles to be carried out at very low temperatures, where such grains would be thermally stable and able to carry a remanence. Therefore we have developed an alternative approach based on low-temperature DC demagnetization of saturation IRM (SIRM), using a vibrating sample magnetometer (VSM; Princeton Measurements Model 3900 MicroMag) equipped with a liquid helium cryostat, enabling measurements down to 10 K.

[22] The magnetization and "demagnetization" processes involved are much less selective than those used by *Dunlop* [1965], and consequently we require a significantly different approach to processing the data in order to map out the grain distribution. A saturating field applied and removed isothermally at a specified temperature T_3 magnetizes the entire thermally stable population at that temperature, i.e., all the grains with (V, H_{K0}) plotting above and to the right of the zero-field blocking contour for T_3 (Figure 1b). Subsequent application and removal of a reverse-polarity DC field H_1 flips the magnetic moments of grains with (V, H_{K0}) plotting below and to the left of the blocking contour for T_3, H_1 (Figure 1b). Each DC backfield treatment similarly reverses the moments of grains plotting in a region of the diagram bounded by two blocking field contours for the specified temperature. Thus the change in remanence ΔM_{Ri} produced by each treatment i can be equated with the remanence contribution of the set of grains lying in this bounded region Ω:

$$\Delta M_R = \int_{\Omega} f(V, H_{K0})\, d\Omega$$
$$\Omega = \{V, H_{K0} | H_{i-1} \leq H_B \leq H_i\}. \quad (11)$$

This region is indicated by the hatched area shown in Figure 1b for $i = 1$. Note that (11) implicitly defines $f(V, H_{K0})$ as the SIRM contribution per unit area on the Néel diagram, which is proportional to the total volume of grains that have individual volumes between V and $V + dV$ and zero Kelvin microscopic coercivities between H_{K0} and $H_{K0} + dH_{K0}$.

[23] The inverse problem of calculating $f(V, H_{K0})$ from a DC backfield remanence data set $M_R(H_{DC}, T)$ can be heuristically linked to the tomographic imaging problem

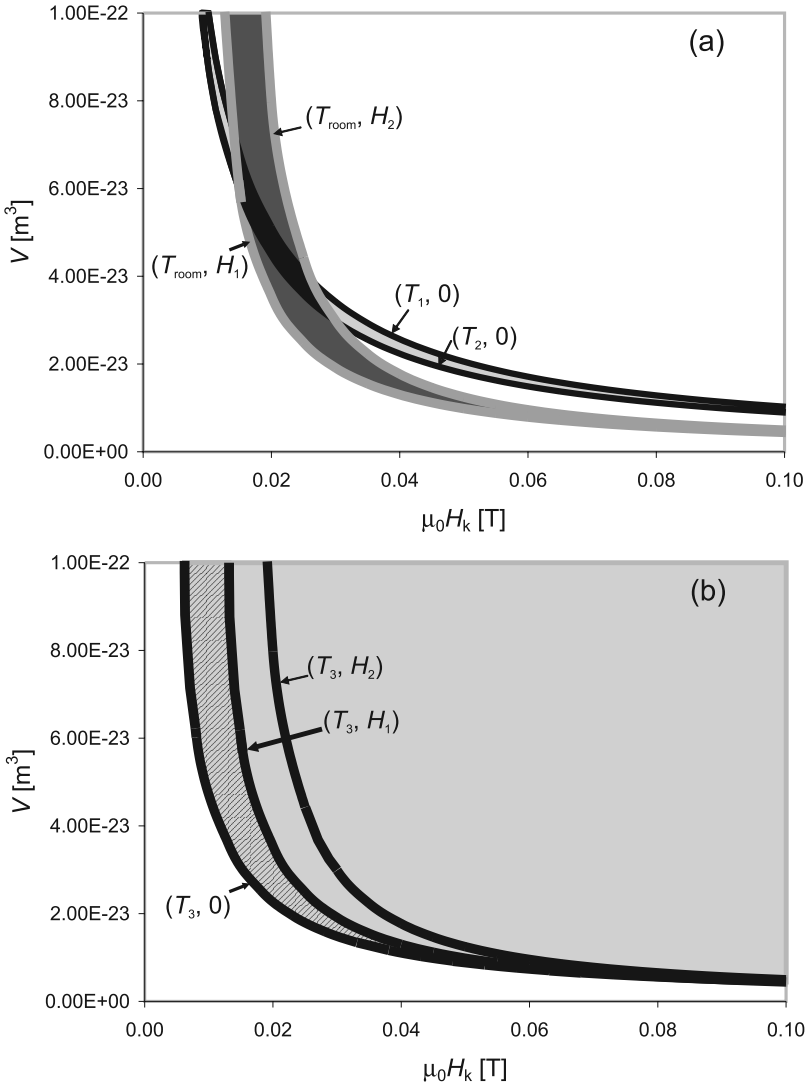

Figure 1. (a) Schematic illustration of *Dunlop*'s [1965] selective magnetization/demagnetization approach for reconstructing $f(V, H_{K0})$. A pTRM imprinted over the temperature interval (T_1, T_2) selectively magnetizes grains with (V, H_{K0}) in the region between the low-field blocking contours for T_1 and T_2 (light gray and black shading). Subsequent stepwise AF demagnetization progressively erases this pTRM from left to right; the magnetization removed between H_1 and H_2 is carried entirely by grains with (V, H_{K0}) in the black-shaded area, and the magnitude of the remanence loss indicates the average value of $f(V, H_{K0})$ over that small and well-defined area. (b) Magnetization/demagnetization processes we use for our technique are less selective: A strong field IRM imprinted at temperature T_3 is carried by the entire thermally stable population at that temperature (gray shaded area); A DC backfield H_1 applied and removed at T_3 reverses the moments of grains in the hatched area.

by imagining the area integrals (11) to collapse to line integrals in the limit $\partial M_R/\partial H_{DC} = \lim_{\Delta H_{DC}\to 0} \Delta M_R/\Delta H_{DC}$ when we differentiate the backfield curves:

$$\partial M_R/\partial H_{DC} = \int_{\Gamma} f(V, H_{\mathrm{K0}})\, \mathrm{d}\Gamma, \qquad \Gamma = \{V, H_{\mathrm{K0}} | H_{\mathrm{B}} = H_{\mathrm{DC}}\}. \tag{12}$$

Tomography can be generally defined as the reconstruction of a two- or three-dimensional distribution from a collection of measured line integrals along paths that sample the distribution with sufficient spatial coverage and with a suitable range of "viewing" angles. Most commonly, the distribution sought is the spatial variation in a physical property such as seismic P wave velocity (e.g., $V_p(x, y, z)$); each measured traveltime represents the line integral of slowness (reciprocal velocity) along a particular ray path. Here we wish to determine the statistical distribution of grain characteristics in a parameter space, $f(V, H_{K0})$, but the inverse problem is mathematically equivalent, because the measured data represent line integrals of the distribution to be determined.

[24] In practice, we find that the one-dimensional approximation (12) is not sufficiently accurate for the forward calculations, and we use (11) or its discrete equivalent.

Nevertheless the inverse problem can still be addressed using the methods of tomography. We use an iterative algebraic inversion technique similar to that described by *Spakman and Nolet* [1988] [see also *Kak and Slaney*, 1988]. We specify an arbitrary starting model ${}^0f(V, H_{K0})$, for which we can calculate expected back-field remanence spectrum curves ${}^0\Delta M_R(H_{DC}, T)$ by numerical integration of equation (11). For each individual measurement $\Delta M_{Ri}(H_{DC}, T)$, we then adjust the model over the region of integration (bounded by the appropriate blocking contours), by an amount proportional to the difference between measured and predicted values. After adjustments for all measured values we have an improved model ${}^1f(V, H_{K0})$, and the next iterative cycle begins with forward calculations yielding the synthetic data set ${}^1\Delta M_R(H_{DC}, T)$. These iterations are repeated a prescribed number of times (typically on the order of 100) or until specified goodness-of-fit criteria are met.

[25] In detail, the calculations involve a discrete representation of $f(V, H_{K0})$. We divide the Néel diagram into a rectilinear grid of cells, within each of which f is uniform. Because we are interested in volumes spanning several orders of magnitude (for magnetite, roughly 10^{-25} to 10^{-21} m^3), we scale the V axis logarithmically. The discrete equivalent of equation (11) is

$$\Delta M_{Ri} = \sum_{j=1}^{n_{cells}} f_j a_{ij}. \tag{13}$$

Here ΔM_{Ri} is the ith measured remanence difference, f_j is the value of the function f for the jth cell in the grid, and a_{ij} is the area of cell j within the area bounded by the blocking contours for the temperature and applied DC fields used in measuring ΔM_{Ri} (see below for a description of how this area is calculated).

[26] The matrix a thus encapsulates the physics of the problem (i.e., the relationship between grain characteristics V and ΔN, intrinsic mineral properties $M_S(T)$, experimental conditions T and H_{app}, and measurable changes in remanence ΔM_R). It is calculated once and then remains unchanged by the iterative adjustments to the $f(V, H_{K0})$ model. To construct H_B contours for each temperature we evaluate

$$\begin{aligned} H_B(V, H_{K0}, M_{S0}, T, \beta[T], \tau_m) &= 0.524 H_K(H_{K0}, \beta[T]) \\ &- H_q(V, H_{K0}, M_{S0}, T, \beta[T], \tau_m) \end{aligned} \tag{14}$$

for the (V, H_{k0}) coordinates of each node in the grid, using equation (8) for calculation of H_q, and using a specified model of $M_S(T) = M_{S0}\beta(T)$. Each temperature and applied field pair (T, H_{app}) represented in the data set corresponds to a unique blocking contour, defined as the locus of (V, H_{K0}) for which $H_B(T, V, H_{K0}) = H_{app}$. We calculate the intersection points of the contours with the grid lines by linear interpolation between nodes, and we approximate the contours by straight-line segments between these intersection points in calculating the areas a_{ij}.

[27] In most cases we use a uniform starting model with ${}^0f_j = 0$ for all j. In order to evaluate resolution and uniqueness, it is useful to repeat the inversion using a variety of different starting models, and for this purpose we also employ 2-D Gaussian distributions and nonzero constant distributions. The starting model is used to generate a synthetic data set according to (13), and residuals are calculated as the difference between measured and synthetic data:

$${}^sR_i = \Delta M_{Ri,measured} - {}^s\Delta M_{Ri,calculated}, \tag{15}$$

where s is the iteration number. The model is then adjusted by "back-projecting" the residuals [*Kak and Slaney*, 1988]:

$${}^s\Delta f_{ij} = \frac{{}^sR_i a_{ij}}{\sum_{k=1}^{n_{cells}} a_{ik}^2}. \tag{16}$$

For each measurement i, the adjustment applied to cell j is proportional to R_i and to the area of the cell lying within the integration area. The updates are applied after they have all been calculated for the current iteration (simultaneous iterative reconstruction technique [*Kak and Slaney*, 1988]):

$${}^{s+1}f_j = {}^sf_j + \frac{C}{n_{measurements}} \sum_{i=1}^{n_{measurements}} {}^s\Delta f_{ij} (j = 1..n_{cells}). \tag{17}$$

The dimensionless constant C in (17) is used to control the rate of convergence; higher values generally cause the iterative process to converge to a solution more rapidly, but excessive values can cause the process to become unstable and diverge.

2.7. Rigorous Forward Model With Random Orientations

[28] In the forward calculations used in our tomographic modeling (equations (11) and (14)) we only partially account for differences between an aligned population and a more realistic randomly oriented population. Specifically, in comparison with an aligned population, a randomly oriented population of identical noninteracting grains has both a lower average switching field and a broader distribution of switching fields; our tomographic inversion calculations account for the reduced average value but not for the broadened distribution. Here we compare the results of these simplified forward calculations with those of a more rigorous model, in order to evaluate the effects of the simplifications.

[29] We begin with an analytically defined lognormal distribution of sizes and an orthogonal normal distribution of microcoercivities (Figure 2a). For the forward model we assume an infinite set of noninteracting, uniaxial particles with a random orientation distribution, and we adopt the most detailed thermal fluctuation model currently known. The magnetization of the sample as a function of time is given by

$$M(t) \propto \int_0^{\pi/2} m(t, \varphi) \sin 2\varphi \, d\varphi, \tag{18}$$

where $m(t, \varphi)$ is the magnetic moment of all particles whose easy axes are at an angle φ with respect to the applied field. The time evolution of the total magnetization of these particles is given by

$$m(t, \varphi) = m_\infty + (m_0 - m_\infty) e^{-ft}, \tag{19}$$

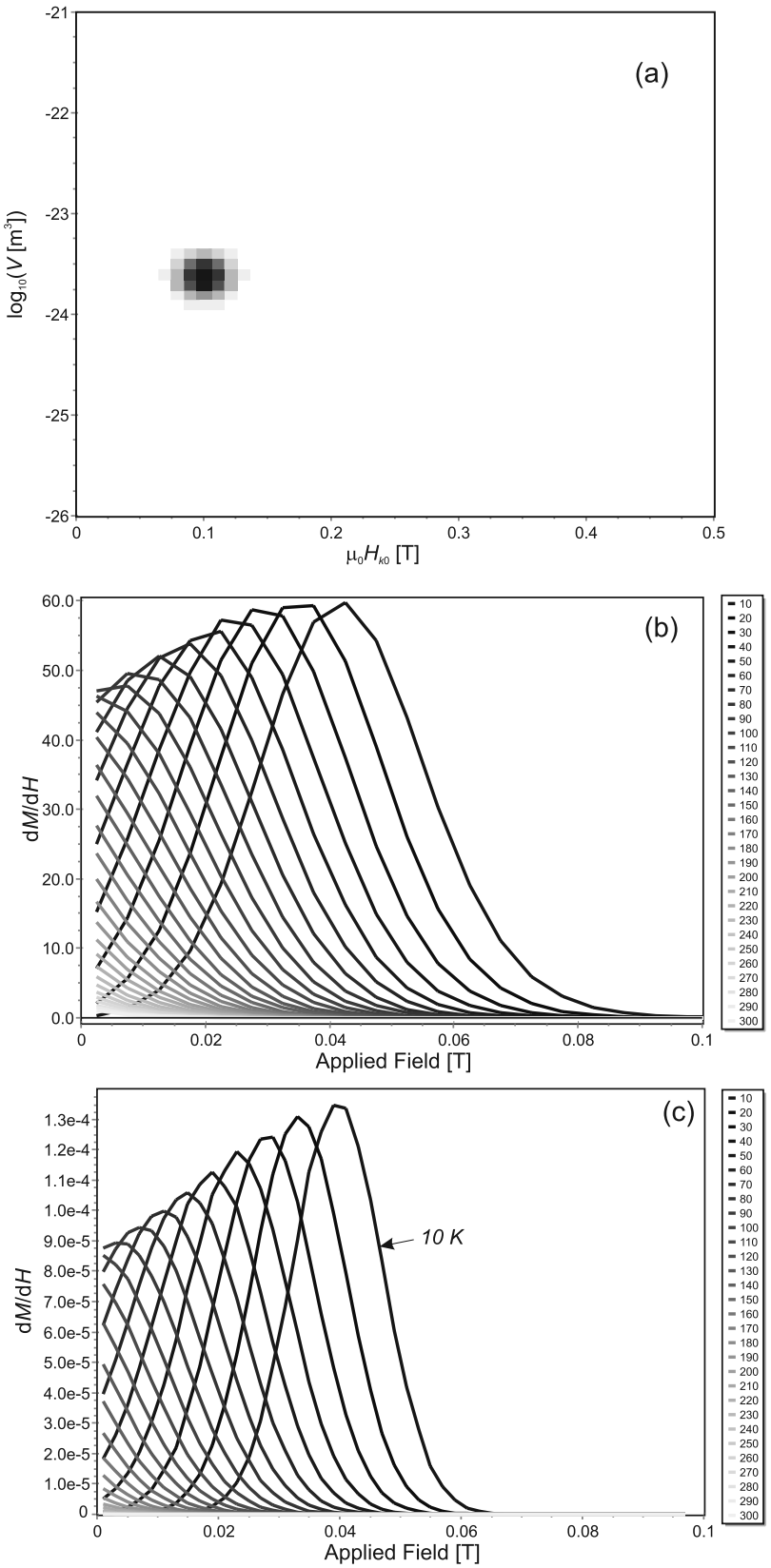

Figure 2. (a) Synthetic $f(V, H_{K0})$ model with $\langle V \rangle = 2.4 \times 10^{-24}$ m^3; standard deviation is 0.2 log units; $\mu_0 \langle H_{K0} \rangle = 100$ mT; standard deviation is 20 mT. (b and c) Backfield remanence spectra calculated using the $f(V, H_{K0})$ model in Figure 2a, assuming $T_C = 850$ K, $M_{S0} = 480$ kA/m, and $\gamma = 0.43$, and using a rigorous model (Figure 2b) that accounts for the angular dependence of thermally assisted switching for a randomly oriented population of identical grains, or using a simplified model (Figure 2c) in which the angular dependence is incompletely addressed.

where f is the switching frequency of the particles, t the time elapsed in the same configuration (i.e., applied field and zero field), $m_0 = m(t = 0)$, and

$$m_\infty = m(t \to \infty) = \tanh\left(\frac{\mu_0 V M_S H_{app}}{kT}\right) \tag{20}$$

with H_{app} being the applied field (a positive saturating field during acquisition, a negative field at each backfield step, and zero during the measurements). We use the thermal activation model of *Brown* [1959, 1963] to calculate the switching frequencies in zero field (f_z) and in applied field (f_a). Following *Dormann et al.* [1997], we obtain

$$\begin{aligned} f_z &= 2F_0\mu_0 H_K \lambda^{1/2}\varepsilon^{3/2}\exp(-\lambda\varepsilon) \\ f_a &= f = F_0\mu_0 H_K \lambda^{1/2}\varepsilon^{3/2}\exp(-\lambda\varepsilon) \end{aligned} \tag{21}$$

with $F_0 = 2\gamma_0/\sqrt{\pi} \approx 99.2$ GHz/T, $\lambda = \mu_0 M_s V H_K/(k_B T)$, and ε is a numerical factor that accounts for the actual value of the energy barrier. In zero field $\varepsilon = 1/2$, and f_z in equation (21) equals $1/\tau$ in (5), with $H_{app} = 0$ and $\tau_0^{-1} = 2F_0\mu_0 H_K \lambda^{1/2}\varepsilon^{1/2}$. In an applied field, ε cannot be calculated analytically; *Egli and Lowrie* [2002] obtained the following approximation:

$$\varepsilon(H,\varphi) = \left(\frac{2}{3}\right)^{3/2} \sin 2\theta_{sw}\left(1 - \frac{H}{H_{sw}}\right)^{3/2}, \tag{22}$$

$$H_{sw} = H_K \frac{\sqrt{1 - t^2 + t^4}}{1 + t^2}, \quad t = \tan^{1/3}\varphi, \tag{23}$$

$$\tan\theta_{sw} = \frac{\sqrt{3} - \sqrt{4h_{sw} - 1}}{2\sqrt{1 - h_{sw}^2}}, \tag{24}$$

where $h_{sw} = H_{sw}/H_k$ and θ_{sw} is the angle at which the moment switches irreversibly. Equation (22) becomes exact as $H \to H_{sw}$.

[30] For the synthetic $f(V, H_{k0})$ model (Figure 2a), we calculate backfield remanence curves over the temperature interval 10–300 K, using both the rigorous approach (equations (18)–(24)), and the simplified approach ((13) and (14)). As expected, the backfield distributions calculated with the rigorous model (Figure 2b) are broader than those calculated with the simplified calculations (Figure 2c). In all other respects, however, the synthetic backfield data sets have the same essential character: with increasing temperature the peaks shift to lower fields and decrease in height, and the shifts occur at the same rate in both cases.

2.8. Predicting $\kappa(f, T)$ Using Calculated $f(V, H_{K0})$

[31] Once the grain distribution has been determined, it can be used to calculate the behavior expected in other experiments. For example, *Dunlop* [1965] calculated $f(V, H_{K0})$ from AF demagnetization of a set of weak field pTRMs, and then used it to predict the thermal demagnetization spectra of pTRMs acquired in different DC fields. Here we use the grain distributions obtained from thermal fluctuation tomography to model the frequency and temperature dependence of susceptibility, $\kappa(f, T)$, using Néel theory [*Néel*, 1949; see also *Worm and Jackson*, 1999; *Shcherbakov and Fabian*, 2005].

[32] The equilibrium magnetization M_{eq} reflects a balance between the aligning influence of an external field and the randomizing effects of thermal energy. For an aligned assemblage of SP or SSD particles in an applied field H_{app}, the equilibrium magnetization is:

$$M_{eq}(V, M_s, H_{app}, T) = M_s \tanh(\alpha) = M_s \tanh\left(\frac{\mu_0 V M_s(T) H_{app}}{kT}\right). \tag{25}$$

For a randomly oriented assemblage,

$$M_{eq} = M_s L(\alpha) = M_s[\coth(\alpha) - 1/\alpha], \tag{26}$$

which for small α approximates to $\mu_0 V M_s^2 H_{app}/(3kT)$, one third the small α value for the aligned assemblage. The in-phase susceptibility is

$$\kappa' = \frac{M_{eq0}}{H_0(1 + \omega^2\tau^2)} = \frac{\kappa_{eq}}{1 + \omega^2\tau^2}, \tag{27}$$

and the out-of-phase (also known as quadrature or imaginary) component is

$$\kappa'' = \frac{\omega\tau M_{eq0}}{H_0(1 + \omega^2\tau^2)} = \frac{\omega\tau\kappa_{eq}}{1 + \omega^2\tau^2}, \tag{28}$$

where $\kappa_{eq} = \mu_0 V M_s^2/(3kT)$ and τ is given by equation (5) with $H_{app} \sim 0$.

[33] Equations (27) and (28) describe the thermally activated component of susceptibility, i.e., the part due to irreversible rotation of moments over anisotropy energy barriers into minimum energy orientations along the applied field. These components vanish for sufficiently high frequencies and/or long relaxation times ($\omega\tau \gg 1$), i.e., for the SSD state. The quadrature component also vanishes for sufficiently low frequencies and/or short relaxation times ($\omega\tau \ll 1$), i.e., the "pure" SP state, where κ' becomes equal to the equilibrium (DC) susceptibility κ_{eq}. It is in the transitional region between these states ($\omega\tau \sim 1$) that AC behavior is most interesting, with significant frequency dependence and nonmonotonic temperature dependence.

[34] Given a discrete model of the grain distribution $f(V, H_K)$, we can use equations (27), (28), and (26) to calculate κ' and κ'' as functions of frequency and temperature for each grid cell, using the average values of V and H_K for the cell. We then sum over the whole assemblage, weighted cell-by-cell according to $f(V, H_K)$, to obtain the predicted $\kappa(f, T)$ for the sample.

3. Samples, Measurements, and Conventional Analysis

[35] The basal section of the Tiva Canyon Tuff on Yucca Mountain (Nevada) contains fine titanomagnetite grains that crystallized in a silicate glass matrix during cooling after emplacement [*Schlinger et al.*, 1988, 1991]. Thermomagnetic analyses indicate that these grains are low-titanium titanomagnetites with a composition of $Fe_{3-x}Ti_xO_4$

Table 2. Tiva Canyon Sample Stratigraphy and Grain Characteristics[a]

		Measured Dimensions		Expected Values		Inverted Mode		Modal Dimensions		Inverted Mean		Mean Dimensions	
Sample/Site	Z, m	L, nm	w/L	V, 10^{-24} m^3	$\mu_0 H_{k0}$, mT	V, 10^{-24} m^3	$\mu_0 H_{k0}$, mT	L, nm	w/L	V, 10^{-24} m^3	$\mu_0 H_{k0}$, mT	L, nm	w/L
CS913	1.39	85	0.11	7.43	245.32								
TC04-12-7	1.4												
TC04-12-6	1.1					6.31	190	41.7	0.295	3.21	226	46.4	0.18
CS914	0.98	50	0.17	3.61	228.69	5.01	250	84.6	0.091	4.04	226	49.9	0.18
TC04-12-5	0.8												
TC04-10	0.75												
TC04-11	0.75					5.01	180	36.1	0.326	3.23	213	40.4	0.221
CS915	0.57	37	0.2	2.03	219.70								
TC04-12-4	0.5					3.16	180	31	0.326	2.34	208	34.5	0.238
TC04-12-3	0.3					2	160	23.6	0.39	1.74	215	33.5	0.215
CS916	0.17	18	0.28	0.46	194.73								
TC04-12-2	0.12					1.58	160	21.9	0.39	1.41	206	28.8	0.243
CS917	0.03	15	0.36	0.44	169.42	1	150	17.8	0.422	1.97	179	26.3	0.329
TC04-12-1	0.05												

[a]CS samples/sites are those of *Schlinger et al.* [1991]; TC04 sites were sampled at the same locality by the authors of this paper. Not all samples are analyzed in this paper. Z is the stratigraphic height above the base of the flow, approximately determined by measurements in the field. Measured dimensions L and w/L are the mean grain length and aspect ratio determined by *Schlinger et al.* [1991] from TEM images. V is the volume of a rectangular parallelepiped with the given dimensions ($V = L^3*(w/L)^2$); the volume of an ellipsoid with the same dimensions is approximately half as large. Zero-Kelvin microcoercivities are calculated as $\Delta N M_{S0}$ using the demagnetizing factor formula of *Stoner* [1945] and assuming $M_{S0} \sim 420$ kA/m.

($x \sim 0.10$ or TM10). Careful transmission electron microscopy (TEM) studies [*Schlinger et al.*, 1991] and numerous magnetic investigations [*Schlinger et al.*, 1991; *Rosenbaum*, 1993; *Worm and Jackson*, 1999; *Egli and Lowrie*, 2002; *Shcherbakov and Fabian*, 2005] have shown that at each stratigraphic level the distribution of grain sizes and shapes is very narrow, and that it closely approximates a Stoner-Wohlfarth population of identical, randomly oriented elongate grains. Sizes increase from approximately $5 \times 5 \times 15$ nm ($4.5 \times 10_{-25}$ m^3) to $25 \times 25 \times 250$ nm (1.6×10^{-22} m^3) over a 3-m span near the base of the flow (Table 2) [*Schlinger et al.*, 1991]. In this study we have analyzed some of the same samples characterized by *Schlinger et al.* [1991] as well as a new set of samples that we collected in 2004 and 2005 from the same location. The wealth of previous work allows us to rigorously "ground truth" our inversion results.

[36] For purposes of comparison, we also apply thermal fluctuation tomography to (1) a ferrofluid, containing a strongly interacting population of nanoparticles with a narrow distribution of sizes/shapes (Ferrofluidics APG 512 A, nominal particle diameter of 10 nm); and (2) a paleosol sample from the Chinese loess plateau (at Weinan), with a broad range of SP and SSD grain sizes.

3.1. Low-T Hysteresis and Determination of M_{S0} and $\beta(T)$

[37] At the heart of *Dunlop*'s [1965] method and ours is the temperature dependence of H_B (equation (14)), which is controlled by the grain characteristics V and H_{K0}; and by the magnetic mineralogy, which governs M_{S0} and $\beta(T)$. Thus we must begin by determining or assigning values for M_{S0} and $\beta(T)$, and then use field- and temperature-dependent measurements to solve for the distribution of V and H_{K0}.

[38] Experimental determination of M_{S0} and $\beta(T)$ is more complicated for nanophase materials than for thermally stable ones. For the latter, we can attribute the high-field slope of a hysteresis loop entirely to paramagnetism, diamagnetism, and/or antiferromagnetism, and calculate the ferrimagnetic saturation magnetization as the intercept of a best fit line. By measuring hysteresis loops as a function of temperature we determine the saturation moment $m_S(T) = cV_S M_{S0}\beta(T)$, where V_S is the specimen volume and c is the concentration of ferrimagnetic material in the bulk sample. Using the measured values $m_S(T)$ we can fit a function of the form (3) by a suitable choice of γ and T_C, to approximate $\beta(T)$. From the Curie temperature, we estimate the Ti substitution parameter x or the oxidation parameter z from the relations given in *Hunt et al.* [1995], and from this we can estimate M_{S0}.

[39] For populations near or above their blocking temperatures, however, the ferrimagnetic high-field slope may be significantly nonzero [e.g., *Tauxe et al.*, 1996; *Lanci and Kent*, 2003]; the magnetization is no greater than the equilibrium value (26), which may be significantly less than $M_S(T)$. Conventional processing as described above yields an erroneously rapid drop in M_S with increasing T as the strong field equilibrium magnetization diminishes. This is apparent in samples lacking any appreciable paraferromagnetic or antiferromagnetic contribution to high-field slope, and with ferrimagnetic grain sizes of $\sim$10 nm or less, such as the ferrofluid. The rapid drop in the calculated $M_S(T)$ values (Figure 3a, circles) implies either a low T_C or a relatively high γ: we obtain a good fit with $\gamma = 0.66$ and $T_C = 850$ K. However, the addition of a nonlinear term to high-field slope fitting more accurately describes the approach to saturation [*Fabian*, 2006] and yields better values for $M_S(T)$ (Figure 3a, squares). This approach yields parameters appropriate for oxidized magnetite: $\gamma = 0.43$ and $T_C = 880$ K.

[40] For the Tiva Canyon tuff samples (Figure 3b), the paramagnetic contribution to high-field slope is dominant, especially at low temperatures. Moreover, at least for the samples with larger grain sizes and blocking temperatures near or above room temperature, the strong field $M_{eq} \approx M_S$, and the latter can thus be calculated by standard linear regression. Using either linear or nonlinear high-field fits, we obtain $M_S(T)$ that is consistent with $\gamma = 0.43$ and

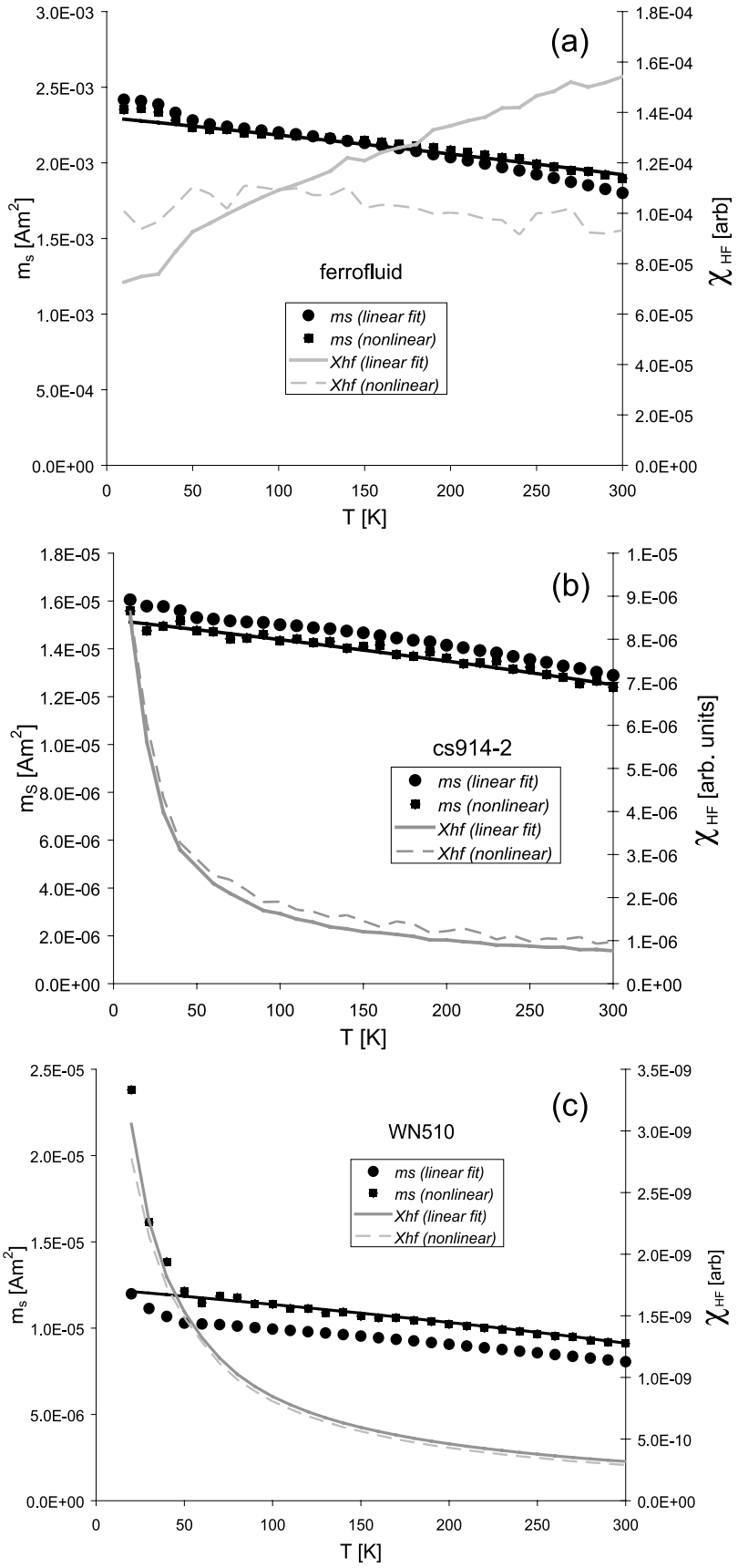
(a)
ferrofluid
ms (linear fit)
ms (nonlinear)
Xhf (linear fit)
Xhf (nonlinear)
m_s [Am^2]
χ_HF [arb]
T [K]
(b)
cs914-2
ms (linear fit)
ms (nonlinear)
Xhf (linear fit)
Xhf (nonlinear)
m_S [Am^2]
χ_HF [arb. units]
T [K]
(c)
WN510
ms (linear fit)
ms (nonlinear)
Xhf (linear fit)
Xhf (nonlinear)
m_s [Am^2]
χ_HF [arb]
T [K]

Figure 3

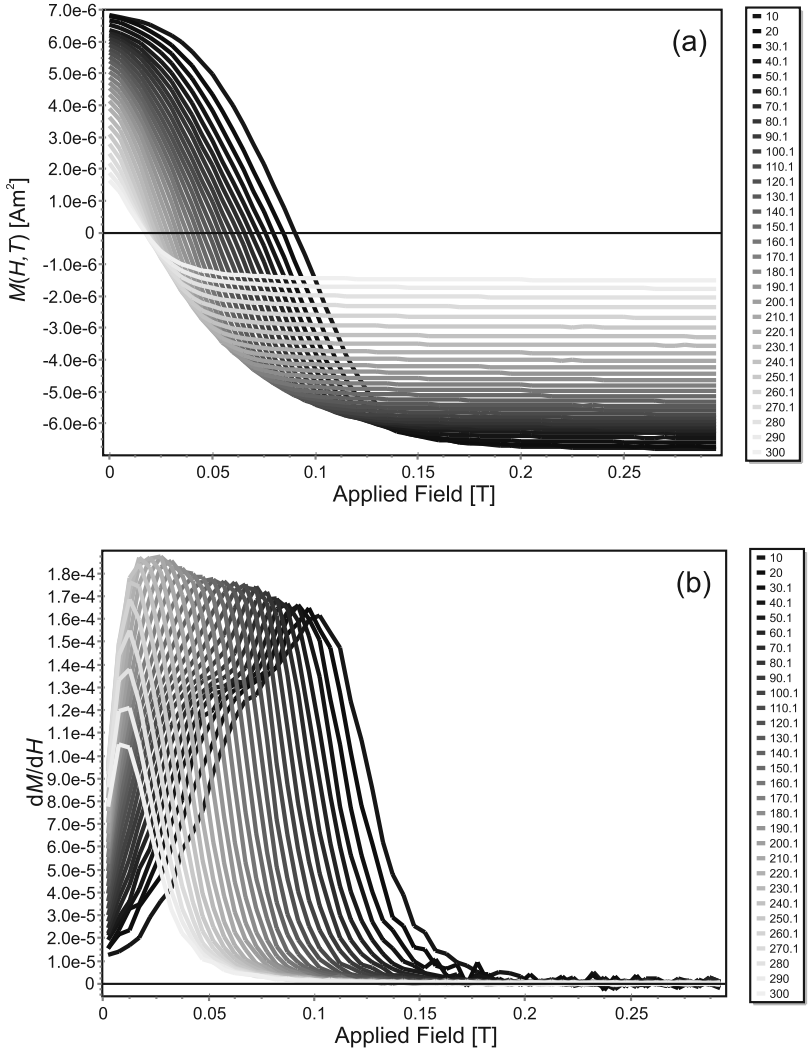

Figure 4. Low-T behavior of sample CS914: (a) remanent magnetization as a function of applied DC backfield and (b) derivative curves. Temperatures from 10 K to 300 K are indicated by gray scale (ΔT = 10); field steps are 5 mT.

T_C = 775 K (502 C), corresponding to an unoxidized composition of approximately TM12 [*Hunt et al.*, 1995]. There is significant uncertainty in the best values for these parameters, since the measurements are all made far below the Curie point, but this composition agrees well with those estimated previously [*Schlinger et al.*, 1988, 1991; *Worm and Jackson*, 1999]. The room temperature mass-specific saturation magnetization for this composition is ~78.4 A m^2/kg [*Hunt et al.*, 1995], which for a density of ~5150 kg/m^3 yields $M_S \sim$ 404 kA/m at room temperature.

[41] In the Weinan paleosol sample the major magnetic phase is presumably maghemite ($T_C \sim$ 645°C = 918 K [*Özdemir and Banerjee*, 1984]) or oxidized magnetite (575°C $\leq T_C \leq$ 645°C). Taking T_C = 900 K, we obtain a good fit using γ = 0.66 for $M_S(T)$ determined by linear high-field fitting, or γ = 0.72 for nonlinear high-field fitting (Figure 3c). Conversely, if we take a lower value for γ (~0.43), an equally good fit is obtained for $M_S(T)$ over this temperature range with $T_C \sim$ 600 K. We emphasize that for our purposes it is not essential to have an exact value for either T_C or γ, as long as the combination used provides an accurate description of $M_S(T)$ over the temperature range of interest. It is interesting to observe that the linear and nonlinear high-field fits yield strongly divergent estimates

Figure 3. Temperature dependence of saturation magnetization for (a) ferrofluid, (b) Tiva Canyon tuff sample CS914, and (c) paleosol WN510. Circles show the saturation moment m_s [A m^2] determined by linear high-field fitting of hysteresis measurements up to 2 T; the gray curve shows the linear high-field slope. Squares show $m_s(T)$ determined by nonlinear high-field fitting. The solid black curve is the analytical approximation $m_s = m_{s0}[(T_C - T)/T_C]^{\gamma}$, based on the nonlinear high-field calculations. Fit parameters are (a) γ = 0.43 and T_C = 880 K (607°C), corresponding to moderately oxidized magnetite; (b) γ = 0.4 and T_C = 775K (502°C), corresponding to an unoxidized composition of approximately TM12; (c) excluding the data below 50 K, γ = 0.72 and T_C = 900 K (627°C), close to maghemite.

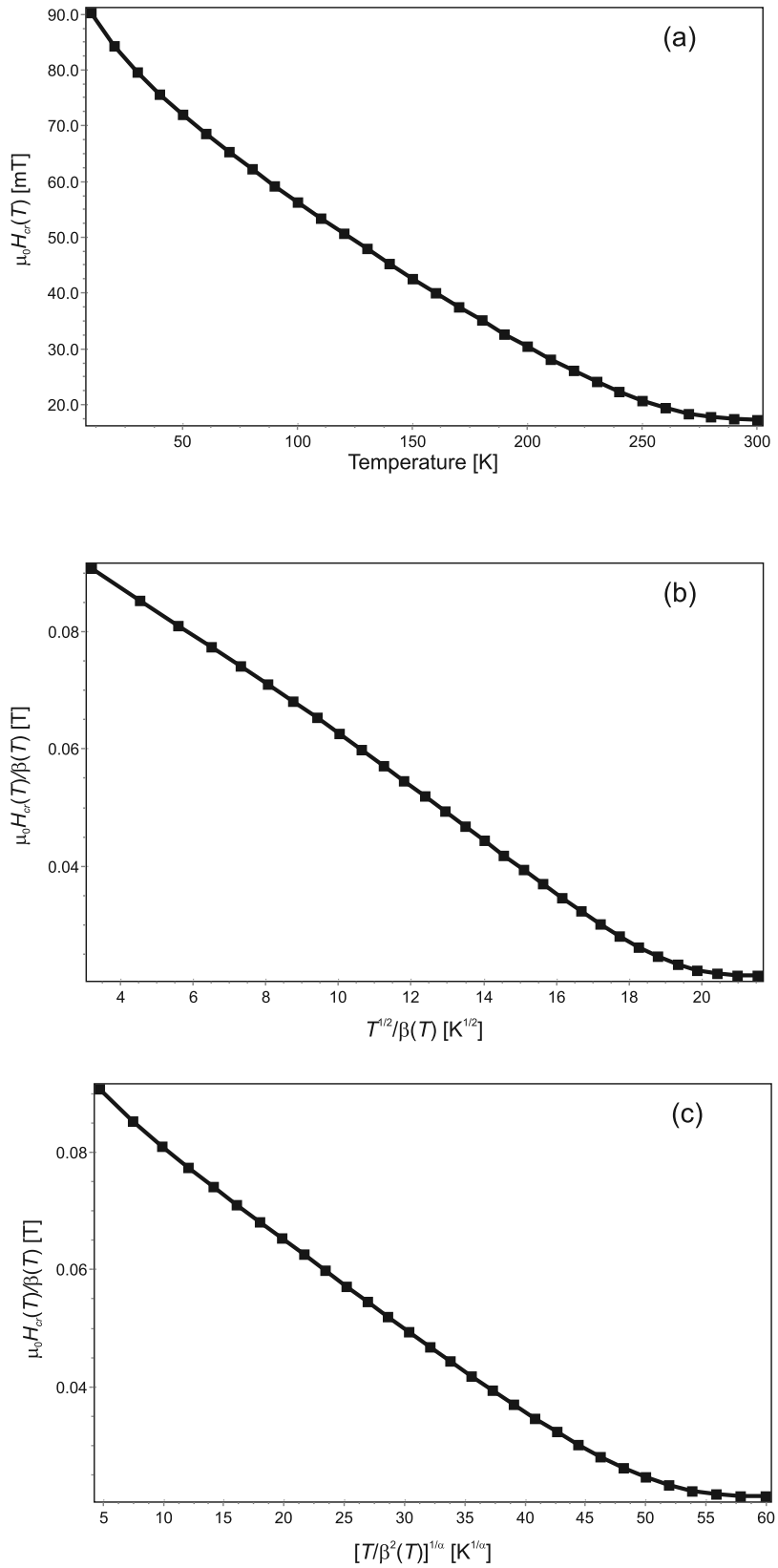
(a)
90.0
80.0
70.0
60.0
50.0
40.0
30.0
20.0
$\mu_0 H_{c1}(T)$ [mT]
50
100
150
200
250
300
Temperature [K]
(b)
0.08
0.06
0.04
$\mu_0 H_{c1}(T)/\beta(T)$ [T]
4
6
8
10
12
14
16
18
20
$T^{1/2}/\beta(T)$ [$K^{1/2}$]
(c)
0.08
0.06
0.04
$\mu_0 H_{c1}(T)/\beta(T)$ [T]
5
10
15
20
25
30
35
40
45
50
55
60
$[T/\beta^2(T)]^{1/\alpha}$ [$K^{1/\alpha}$]

Figure 5

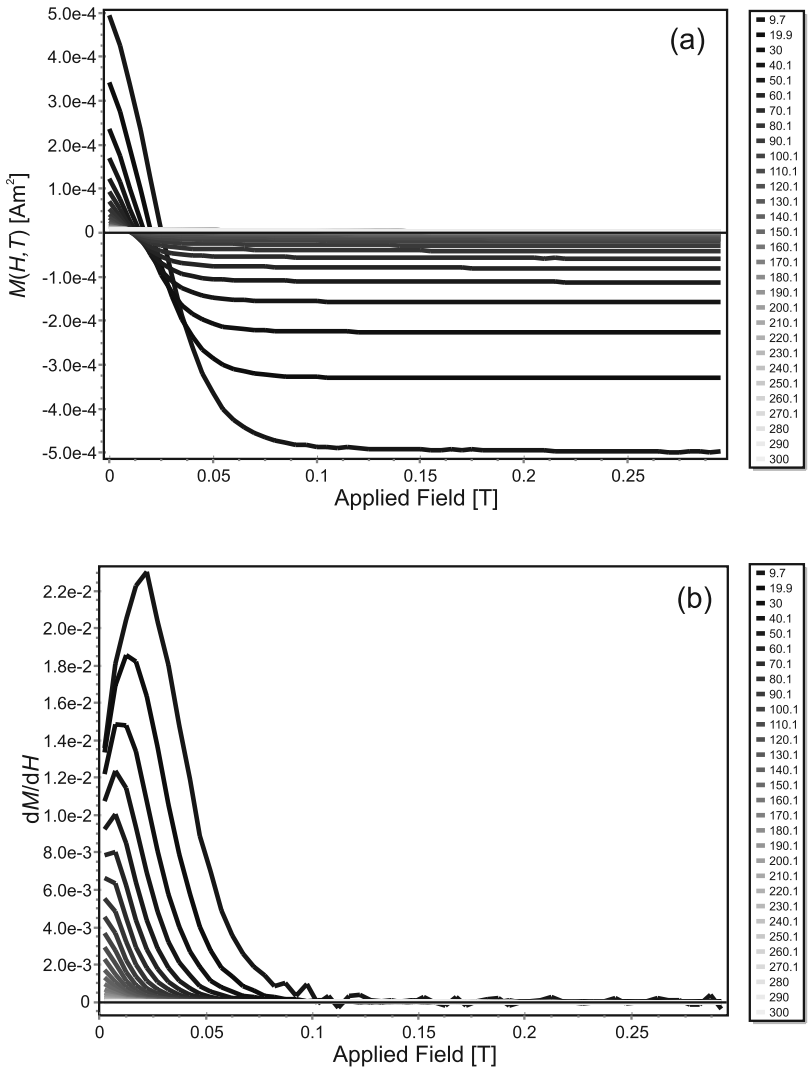

Figure 6. Low-T behavior of ferrofluid sample: Remanent magnetization as a function of applied (a) DC backfield and (b) derivative curves, for temperatures from 10 K to 300 K ($\Delta T = 10$), measured in steps of 5 mT.

of M_S for $T < 50$ K, which appears to be the ordering temperature of a different magnetic phase. For this reason we exclude back-field data for $T < 50$ K from the tomographic analysis for this sample.

3.2. Low-T Backfield Measurements and Thermal Fluctuation Analysis

[42] The back-field remanence curves for the Tiva Canyon samples (e.g., CS914, Figure 4a) exhibit high stability at 10 K (with $\mu_0 H_{cr}$ on the order of 100 mT, and saturation only reached in fields approaching 200 mT), and relatively rapid softening as temperature increases. The back-field derivative curves (Figure 4b) are approximately Gaussian in shape for the lowest temperatures. On warming the curves progressively shift to lower fields and become truncated. The peak heights are roughly constant until they fall sharply at higher temperatures.

[43] The remanent coercivity decreases quasi-linearly for CS914 (Figure 5a), with some curvature at the lowest and highest temperatures. Thermal fluctuation analysis according to equation (9) produces a reasonably straight line, although some curvature remains at the high-temperature end (Figure 5b). The estimated mean grain characteristics are (V, $\mu_0 H_{K0}$) = (1.0×10^{-23} m^3, 103 mT). This is a significantly larger mean grain volume, by a factor of approximately 2.5, than that found for this material

Figure 5. (a) $H_{CR}(T)$ for sample CS914, determined from the data of Figure 4a; (b) thermal fluctuation analysis using equation (9), yielding $\mu_0 H_{K0} = 103$ mT and $V = 1.0 \times 10^{-23}$ m^3; and (c) thermal fluctuation analysis using equation (10), yielding $\mu_0 H_{K0} = 185$ mT and $V = 3.9 \times 10^{-24}$ m^3. In both cases the analysis is adversely affected by nonlinearity at the high-temperature end; limiting the analysis to the interval 10–250 K yields $\mu_0 H_{K0} = 106$ mT, $V = 9.3 \times 10^{-24}$ m^3 (equation (9)) and $\mu_0 H_{K0} = 188$ mT, $V = 3.6 \times 10^{-24}$ m^3 equation (10)).

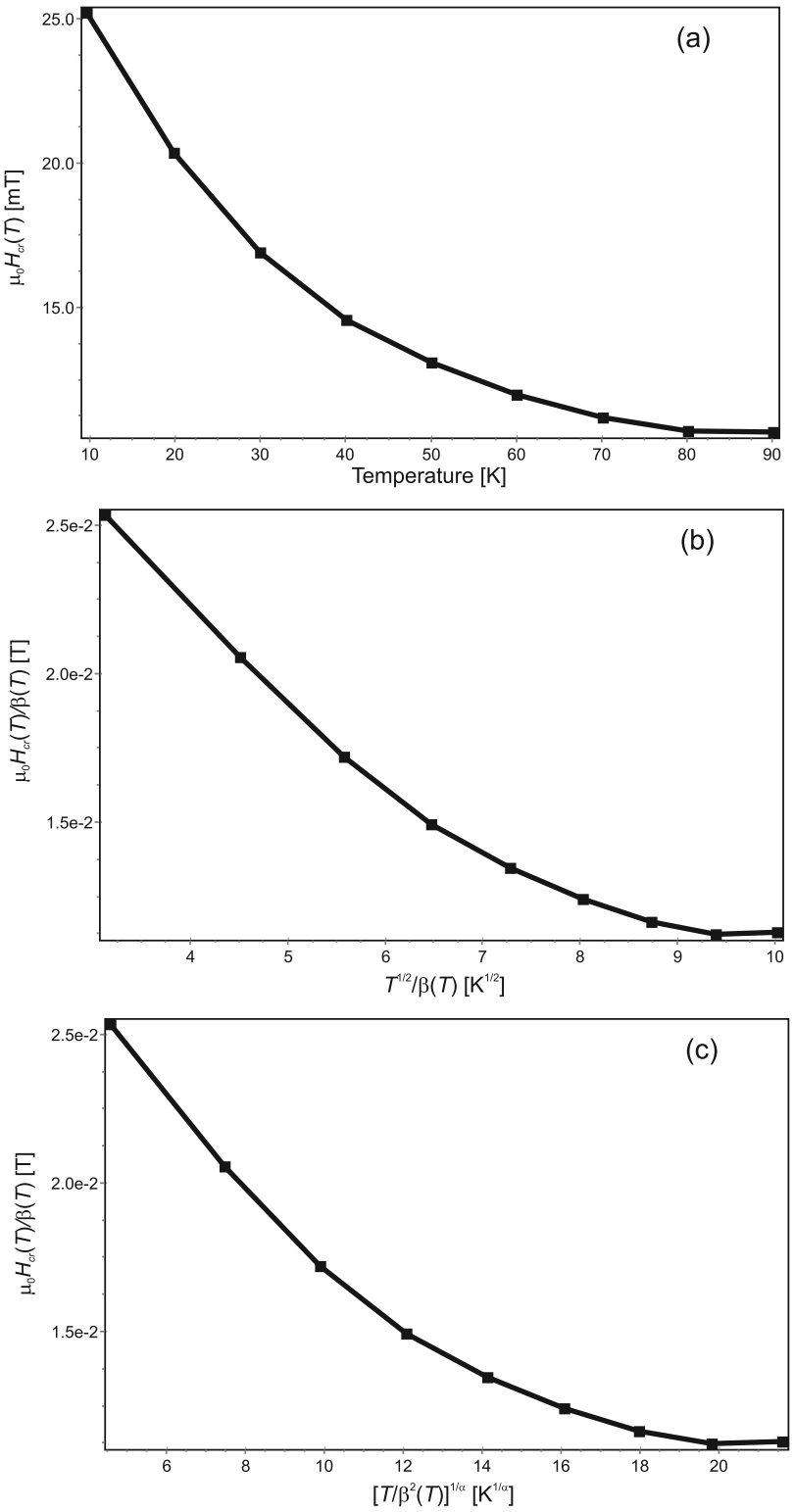

Figure 7. (a) $H_{CR}(T)$ for the ferrofluid sample, determined from the data of Figure 6a. Above 90 K the magnetization is completely unblocked and no meaningful H_{CR} values can be calculated; (b) thermal fluctuation analysis using equation (9), yielding $\mu_0 H_{K0} = 30$ mT and $V = 1.2 \times 10^{-23}$ m^3; (c) thermal fluctuation analysis using equation (10), yielding $\mu_0 H_{K0} = 51$ mT and $V = 5.6 \times 10^{-24}$ m^3. In both cases the strong nonlinearity at all but the lowest temperatures undermines the analysis.

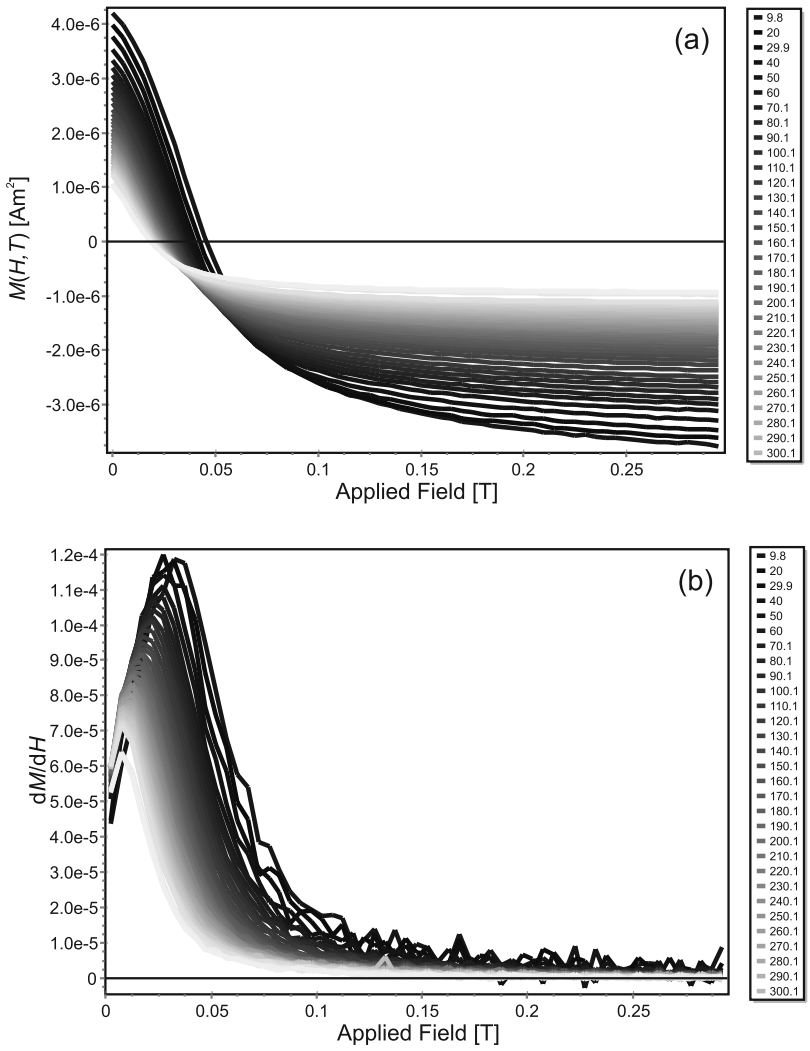

Figure 8. Low-T behavior of the paleosol sample: Remanent magnetization as a function of (a) applied DC backfield and (b) derivative curves, for temperatures from 10 K to 400 K ($\Delta T = 10$), measured in steps of 5 mT.

(Table 2) in previous studies [*Schlinger et al.*, 1991; *Worm and Jackson*, 1999; *Egli and Lowrie*, 2002; *Shcherbakov and Fabian*, 2005]. The disparity is undoubtedly due in part to the diminished slope at higher temperatures, related to a separate population of larger grains. Excluding the data for $T > 250$ K yields a slightly smaller volume and more elongate shape (9.3×10^{-24} m^3, 106 mT). When the analysis is carried out according to equation (10), the calculated mean volume is in better agreement with published estimates (Table 2), and H_{K0} is much larger, although still somewhat low compared to expected values for the observed grain shapes [*Schlinger et al.*, 1991]: (3.9×10^{-24} m^3, 185 mT) for all data and (3.6×10^{-24} m^3, 188 mT) for $T \leq 250$ K.

[44] It is evident in the back-field data and derivative curves (Figure 6) that the ferrofluid contains dominantly finer and less coercive grains. Even at 10 K the remanence saturates by about 100 mT (Figure 6a), and a Gaussian fit to the backfield derivative curves (Figure 6b) would extend well into the negative backfield region. Magnetization is completely unblocked by 80 or 90 K. $H_{CR}(T)$ is strongly curved (Figure 7a), and the curvature largely persists after rescaling for thermal fluctuation analysis (Figures 7b and 7c).

[45] The paleosol data set (Figure 8) suggests a relatively large mean grain size and moderate to weak grain elongations: $\mu_0 H_{CR}$ is less than 50 mT at 10 K, and it shifts downward quite slowly with increasing T. At 400 K there is still a significant thermally stable population of grains. The peaks in the back-field derivative curves (Figure 8b) shift systematically with increasing T to lower fields and reduced peak values. Strongly nonlinear and multiply inflected curves in $H_{CR}(T)$ and thermal fluctuation analysis (Figure 9) suggest a broad and possibly multimodal range of grain sizes and/or shapes.

4. Tomographic Analysis

[46] Our data sets each typically contain 1800 back-field remanence measurements (60 field steps at each of 30 temperatures). These are combined with a $\beta(T)$ model and mapped into blocking contours (Figure 10), successive pairs

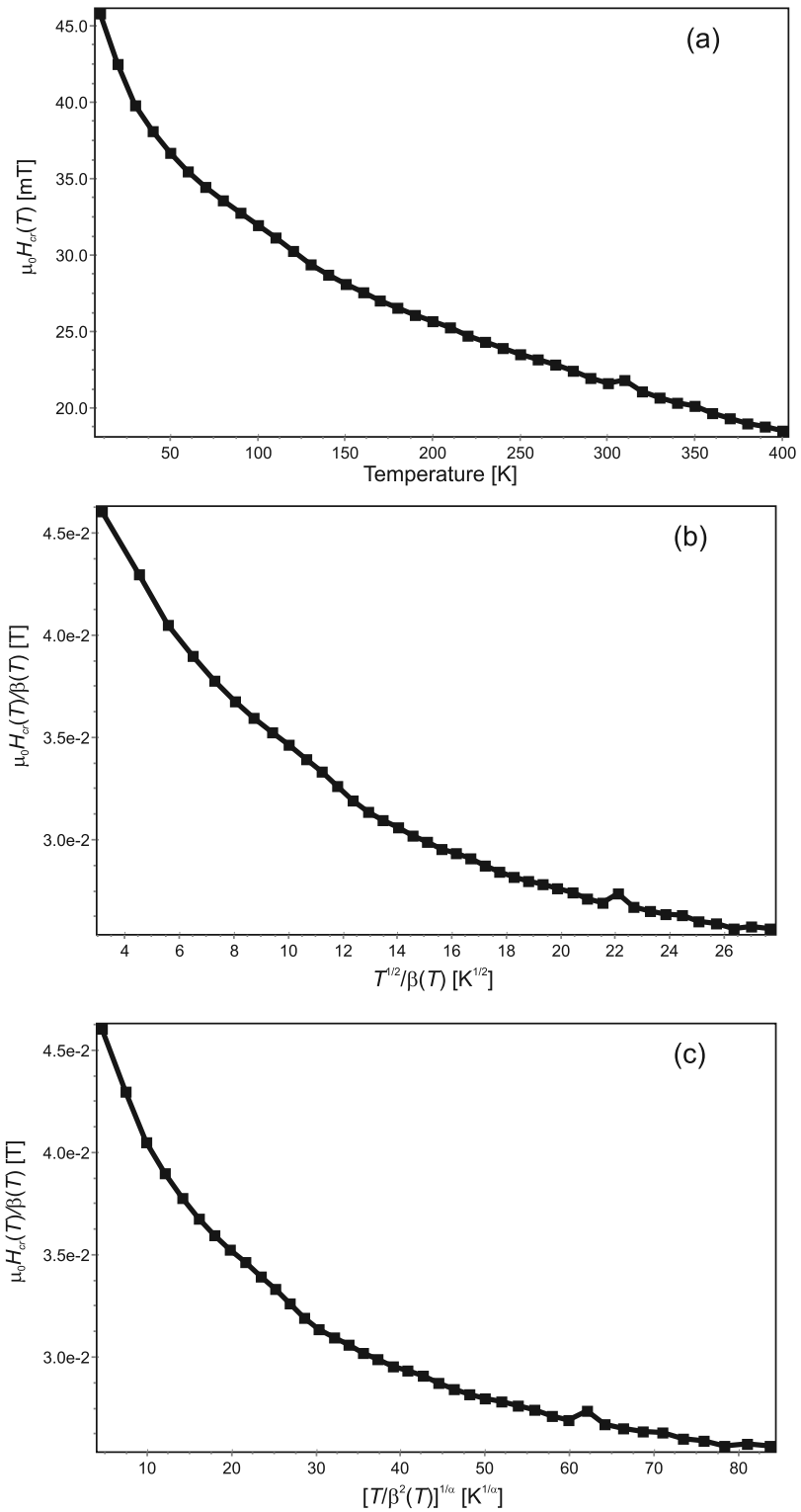

Figure 9. (a) $H_{CR}(T)$ for the paleosol sample, determined from the data of Figure 8a; (b) thermal fluctuation analysis using equation (9), yielding $\mu_0 H_{K0}$ = 42 mT and $V = 1.4 \times 10^{-22}$ m^3; (bottom) thermal fluctuation analysis using equation (10), yielding $\mu_0 H_{K0}$ = 79 mT and $V = 3.4 \times 10^{-23}$ m^3. In both cases the strong nonlinearity probably reflects the broad distribution of sizes.

of which define the regions of integration for equation (11). The density and angular variation in the blocking contours together determine the resolution of the tomographic inversion, in the same way that ray path coverage does in seismic tomography. The ideal situation is to have the entire region crossed by many integration paths in all orientations, and clearly our coverage is less than ideal. First, the blocking contour density is very nonuniform; we may thus anticipate

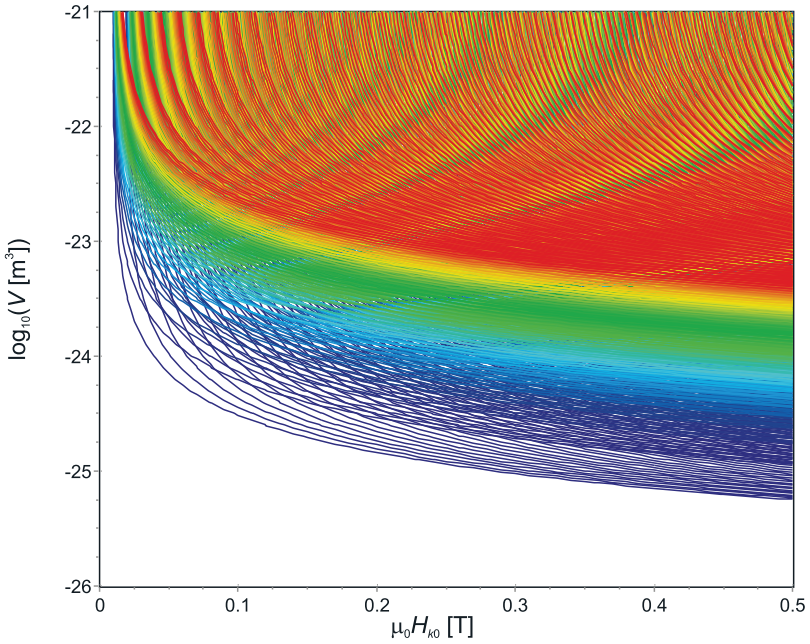

Figure 10. Blocking contours for the fields and temperatures of the data set in Figure 4, calculated assuming shape anisotropy and using $\beta(T) = [(T_C - T)/T_C]\gamma$, with $\gamma = 0.4$ and $T_C = 775$K (502°C), appropriate for the Tiva Canyon samples. Color scale indicates temperatures, from 10 K (blue) to 300 K (red) in 10-degree increments.

no resolution or poor resolution of grain sizes less than a few times 10^{-25} m^3 and microcoercivities less than about 50 mT, where coverage is poor or nil, and increasingly better resolution as particle sizes and/or elongations increase. Second, the range of contour orientations is limited. Because of the physics of thermal activation, the blocking contours necessarily all curve through the Néel plot diagonally from the top edge to the right edge. We can therefore expect some degree of smearing in the reconstructed $f(V, H_{K0})$, parallel to the dominant contour orientation, especially in the poor-resolution areas along the left side and bottom part of the plot.

[47] This is an example of what *Menke* [1984] calls a "mixed determined" inverse problem: overdetermined with respect to some model parameters and underdetermined with respect to others. A hallmark of such problems is an extreme sensitivity of some of the model parameters to noise or small errors in the data, and for this reason it is important to examine the trade-off between fitting errors and length of the solution vector

$$|f| = \left(\sum_{j=1}^{n_{cells}} f_j^2 \right)^{1/2}$$

during convergence.

[48] Because the iterative model corrections are proportional to fitting errors for the previous iteration (equation (16)), these errors decrease quasi-exponentially as the iterative calculations proceed (Figure 11a). For the residuals there is a break in slope after about 100 iterations for the CS914 data set (using $C = 50$ in equation (17)), beyond which the differences between measured and predicted data decrease much more slowly. The rate of change in $|f|$ also decreases after about 100 iterations, but less markedly. Beyond this breakpoint, only marginal improvements are gained in the goodness of fit, while the model parameters continue to change more significantly, and thus to avoid the development of large artifacts in the solution, we generally terminate the process after 100 iterations (or more precisely, after the product $Cn_{\text{iterations}}$ reaches ~5000). The best fit backfield remanence spectra after 100 iterations (Figure 11b) reproduce the essential features of the measured spectra (Figure 4), differing only in fine-scale details. The root-mean-square (RMS) of the residuals (equation (15)), is less than 7% of the RMS of the measured ΔM values.

[49] The reconstructed distribution for CS914 (Figure 12a, 100 iterations) shows a unimodal $f(V, H_{K0})$ distribution, relatively sharply peaked, with a mean $(V, \mu_0 H_{K0}) = (4.0 \times 10^{-24}$ m^3, 226 mT). For this composition, these values correspond to a length 50 nm and a width/length ratio of 0.18, in excellent agreement with the dimensions measured by *Schlinger et al.* [1991] (Table 2). There is a clear elongation of the distribution toward the upper left and lower right, i.e., along the dominant blocking contour orientation. This sort of elongation was also obtained by *Dunlop* [1965] [see also *Dunlop and Özdemir*, 1997], but here it may be due, at least in part, to our processing technique. The distribution extends to microcoercivities exceeding 300 mT, the upper limit for prolate spheroids with magnetite-like magnetizations. There is also a rather pronounced asymmetry in the distribution, with a sharp dropoff toward the upper right and a more gradual decline in the opposite direction. This resembles the asymmetry in the size distributions calculated by *Worm and Jackson* [1999] and by *Shcherbakov and Fabian* [2005]. Interestingly, however, the integrated 1-D volume and microcoercivity distributions here are nearly symmetric (Figures 12b and

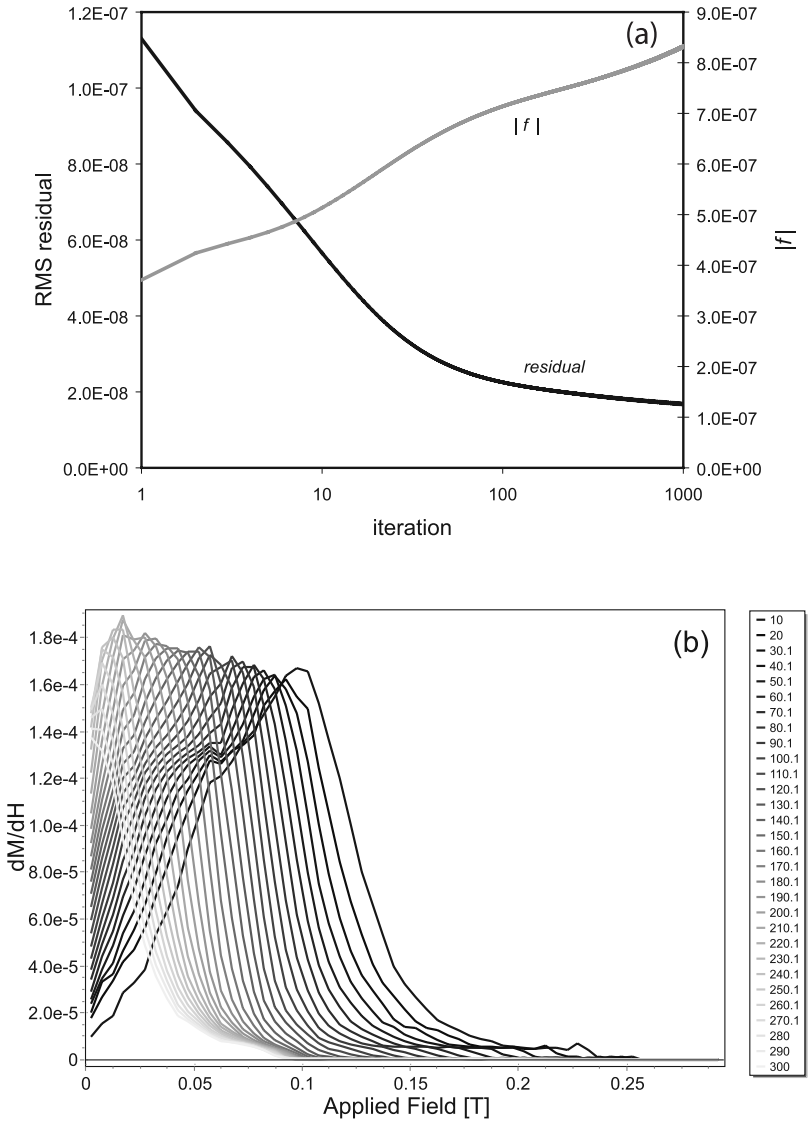

Figure 11. (a) Iterative convergence for Tiva Canyon Tuff sample CS914. Residuals (black curve) decrease quasi-exponentially, rapidly for the first 50 to 100 interations, and more slowly thereafter. The length of the solution vector $|f|$ increases continuously as the peak of the $f(V, H_{K0})$ becomes larger and sharper. (b) Back-field remanence spectra calculated for the $f(V, H_{K0})$ model after 100 iterations. The RMS residual is less than 7% of the RMS measured value.

12c), respectively lognormal and normal. For comparison, a model obtained for the same data set after 1000 iterations (Figure 12d) is somewhat more narrowly peaked but otherwise not significantly different (due to the high signal/noise ratio for this data set).

[50] Susceptibilities calculated using the $f(V, H_{K0})$ model for CS914 agree reasonably well with measured values in their temperature and frequency dependence (Figure 13). The model differs primarily in having higher relative susceptibilities and frequency dependence below 100 K, related to the fine grain size tail visible in Figure 12b. The calculated peaks in κ' and κ'' occur at slightly lower temperatures than those in the measured data set.

[51] One way to evaluate the resolution and uniqueness of this (or any iterative) inverse solution is to use different starting models for the same data set, and see how the final models compare. We show the results of such an analysis in Figure 14 for sample TC04-12-04, approximately the stratigraphic equivalent of CS915 (Table 2), using two initial models: a uniform model with ${}^0f(V, H_{K0}) = 0$ for all cells; and a Gaussian coercivity and log Gaussian volume distribution with a peak at $(V, \mu_0 H_{K0}) = (100 \times 10^{-24}$ m^3, 225 mT). After 100 iterations, each converges to essentially the same final model (Figures 14a and 14b), with a mode at $(V, \mu_0 H_{K0}) = (3.2 \times 10^{-24}$ m^3, 180 mT) and a mean of $(2.3 \times 10^{-24}$ m^3, 208 mT), in good agreement with the expected values. No visible trace remains of the peak of the nonuniform initial distribution. Susceptibility behavior computed for the final model for TC04-12-04 accords well with the observed behavior (Figure 15). As we found for CS914, the peaks in the model occur at slightly lower temperatures than those in the measured data, and the model rather strongly overestimates both susceptibility and its frequency dependence at temperatures below 100 K.

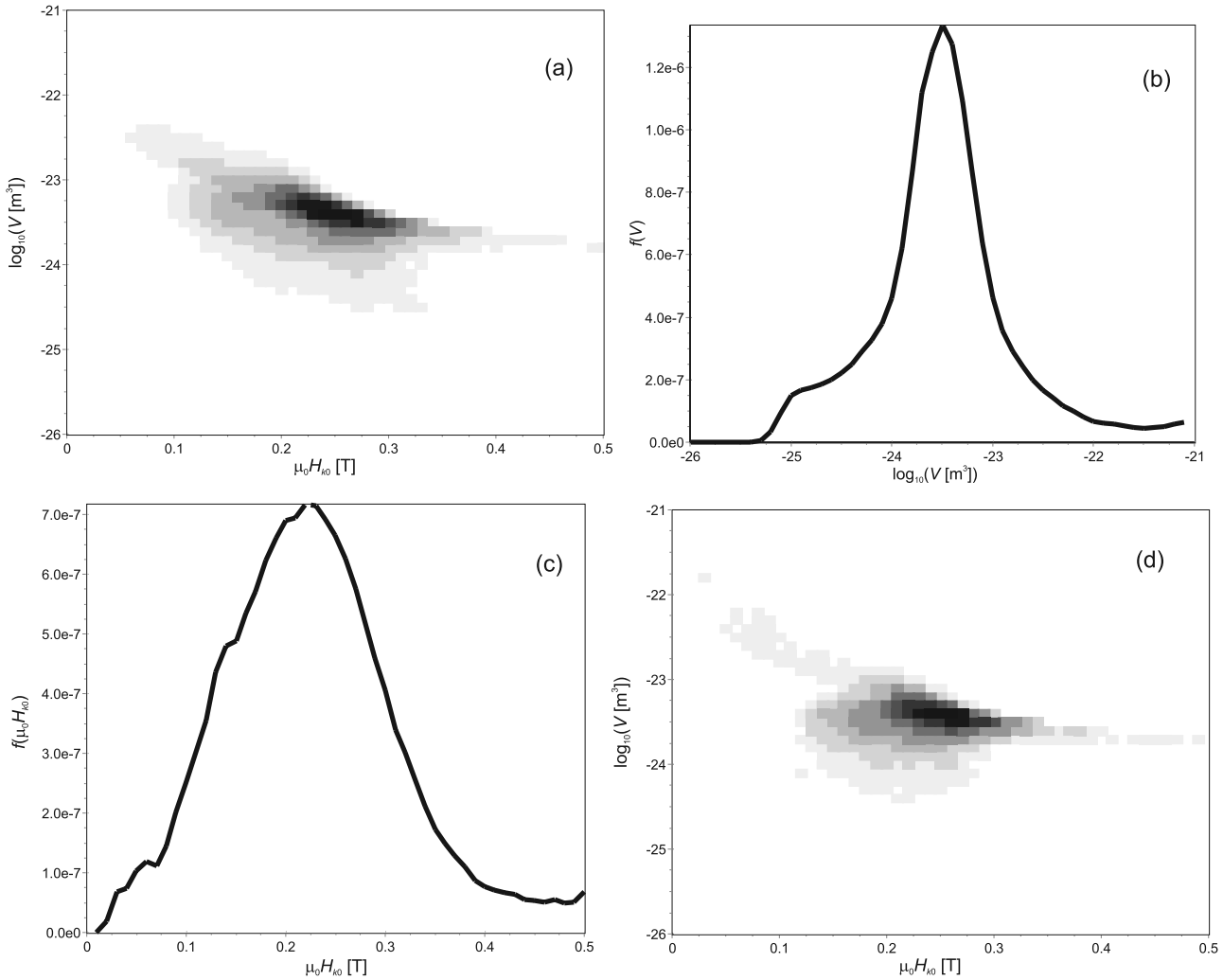

Figure 12. (a) Calculated $f(V, H_{K0})$ for Tiva Canyon Tuff sample CS914, using the data of Figure 4 (contour interval = $f_{max}/10$). The distribution is unimodal, with a mean of $(V, \mu_0 H_{K0}) = (4.0 \times 10^{-24}\ m^3, 226\ mT)$. For this composition, those values correspond to ellipsoidal grains of length 50 nm, with a width/length ratio of 0.18. These are virtually identical to the dimensions determined from TEM images by *Schlinger et al.* [1991]. (b) and (c) Distributions of volume and microcoercivity, obtained by summing the rows and columns of the 2-D model in Figure 12a. (d) The $f(V, H_{K0})$ model after 1000 iterations.

[52] For a direct test of the ability of thermal fluctuation tomography to resolve multimodal populations, we crushed and mixed Tiva Canyon Tuff samples from two levels: TC04-12-3 (stratigraphically approximately equivalent to CS916; Table 2); and TC04-12-6 (approximately equivalent to CS914). The bimodality is subtly expressed in the backfield curves (Figure 16a) and is more apparent in the derivatives (Figure 16b), especially for intermediate temperatures. $H_{CR}(T)$ is strongly nonlinear (Figure 17a), with multiple inflections due to the two nanoparticle populations, and also a coarser third population residing in lithic fragments. Thermal fluctuation analysis (Figure 17b) yields what may be in some sense an average for the three populations, with a larger volume ($10.3 \times 10^{-24}\ m^3$) and lower H_{K0} (121.89 mT) than either of the main components in the mixture.

[53] The calculated grain distribution (Figure 18) shows a clearly bimodal $f(V, H_{K0})$ distribution, with two elongated but relatively sharp peaks, one at $(V, \mu_0 H_{K0}) = (5.2 \times 10^{-24}\ m^3, 210\ mT)$ and a slightly smaller one at $(2.0 \times 10^{-24}\ m^3, 160\ mT)$. These are in reasonable agreement with the expected values (Table 2). It is interesting to note that the trend described by *Schlinger et al.* [1991], with grain size and grain elongation both increasing upsection, is quite evident in the relative positions of the peaks, despite the smearing along the dominant contour orientations.

[54] To evaluate the resolving power in the direction of the dominant contour orientations, we constructed two different (log) Gaussian starting models that have the same product $\langle V \rangle \langle H_{k0} \rangle$ (Figures 19a and 19b). As shown by *Shcherbakov and Fabian* [2005], such distributions cannot be distinguished on the basis of $\kappa(f, T)$ data alone, since the distribution of weak field activation energies is the same for each model, and indeed we find the predicted $\kappa(f, T)$ behavior for these two models to be indistinguishable (Figure 19c). However the predicted response to strong

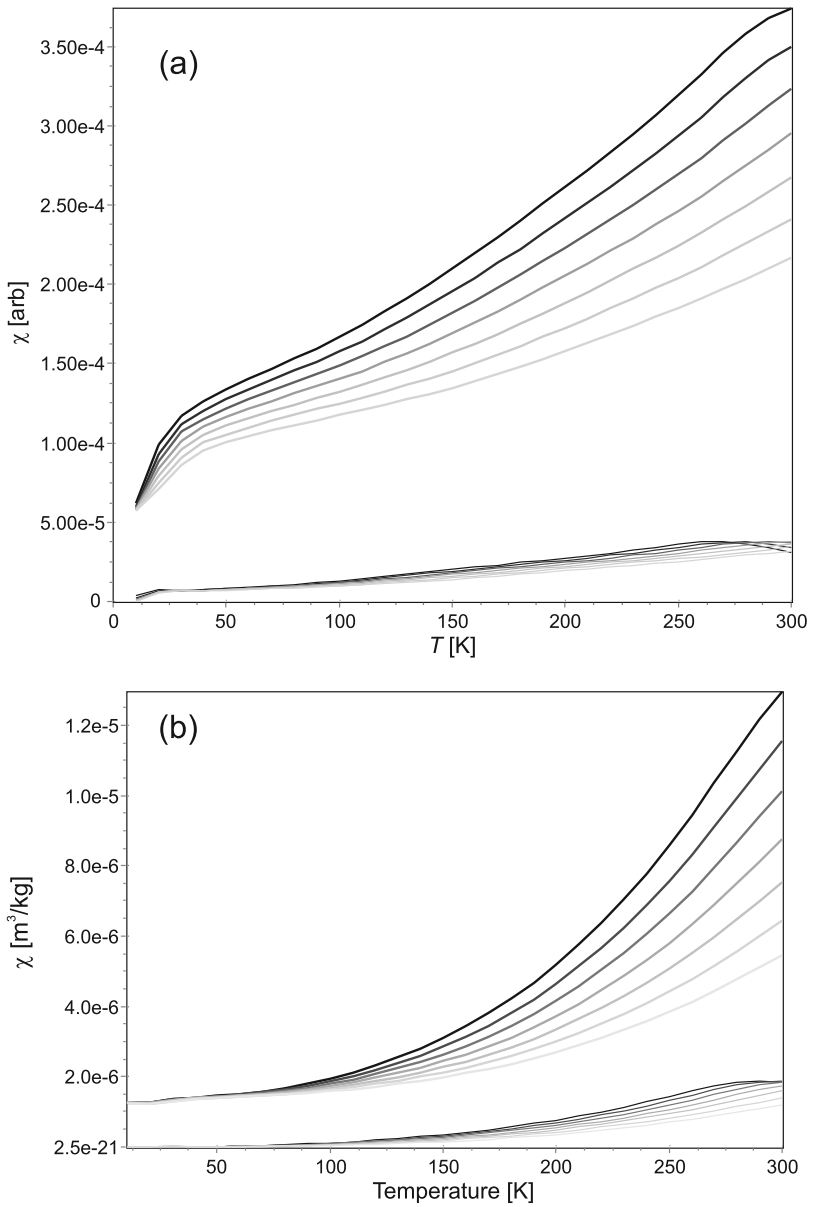

Figure 13. (a) In-phase (bold curves) and quadrature (fine curves) susceptibility calculated for the $f(V, H_{K0})$ model for CS914 (Figure 12a). Gray scale indicates frequency, from 1 Hz (black), through 3.16, 10, 31.6, 100, 316, to 1000 Hz (light gray). (b) Measured susceptibilities.

back fields is quite different for the two distributions (Figures 19d and 19e). When we invert the synthetic data of Figure 19d, using the distribution of Figure 19b as a starting model, the inversion converges (albeit slowly) to one (Figure 20) that more strongly resembles the correct distribution (i.e., that of Figure 19a).

[55] The calculated grain distribution for the Chinese paleosol sample (Figure 21) is much broader than those for the tuff samples, extending from volumes of 10^{-25} m^3 up to 10^{-21} m^3 and beyond, and spanning microcoercivities from 30 to 300 mT. The mode at $(V, \mu_0 H_{K0}) = (12.6 \times 10^{-24}$ m^3, 90 mT) corresponds to a length of 31.8 nm and a width/length ratio of 0.63 (assuming $M_{s0} \sim 420$ kA/m), close to the SP-SSD boundary at room temperature [e.g., *Butler and Banerjee*, 1975]. Calculated susceptibilities (Figure 22a) reflect that, with broad peaks in κ' and κ'' near room temperature and a strong frequency dependence at all temperatures above 50 K. The agreement between calculated (Figure 22a) and measured (Figure 22b) behavior is only moderately good, in part because of a paramagnetic contribution that is significant at the lowest temperatures and that is not included in the modeled behavior. More importantly, the model shows a complete absence of particles with $T_b < 50$ K; this is a consequence of our excluding the backfield data for $T < 50$ K. The inverse calculations populate the model with such low-T_b (small V and/or H_{K0}) particles only where the low-temperature back-field data demand them.

[56] The ferrofluid model (Figure 23a) shows a relatively tight distribution, albeit with considerable elongation along the dominant blocking contour orientation. The mode at $(V, \mu_0 H_{K0}) = (0.8 \times 10^{-24}$ m^3, 90 mT) corresponds (assuming $M_{s0} \sim 490$ kA/m) to particle dimensions of L $\sim$ 14.2 nm,

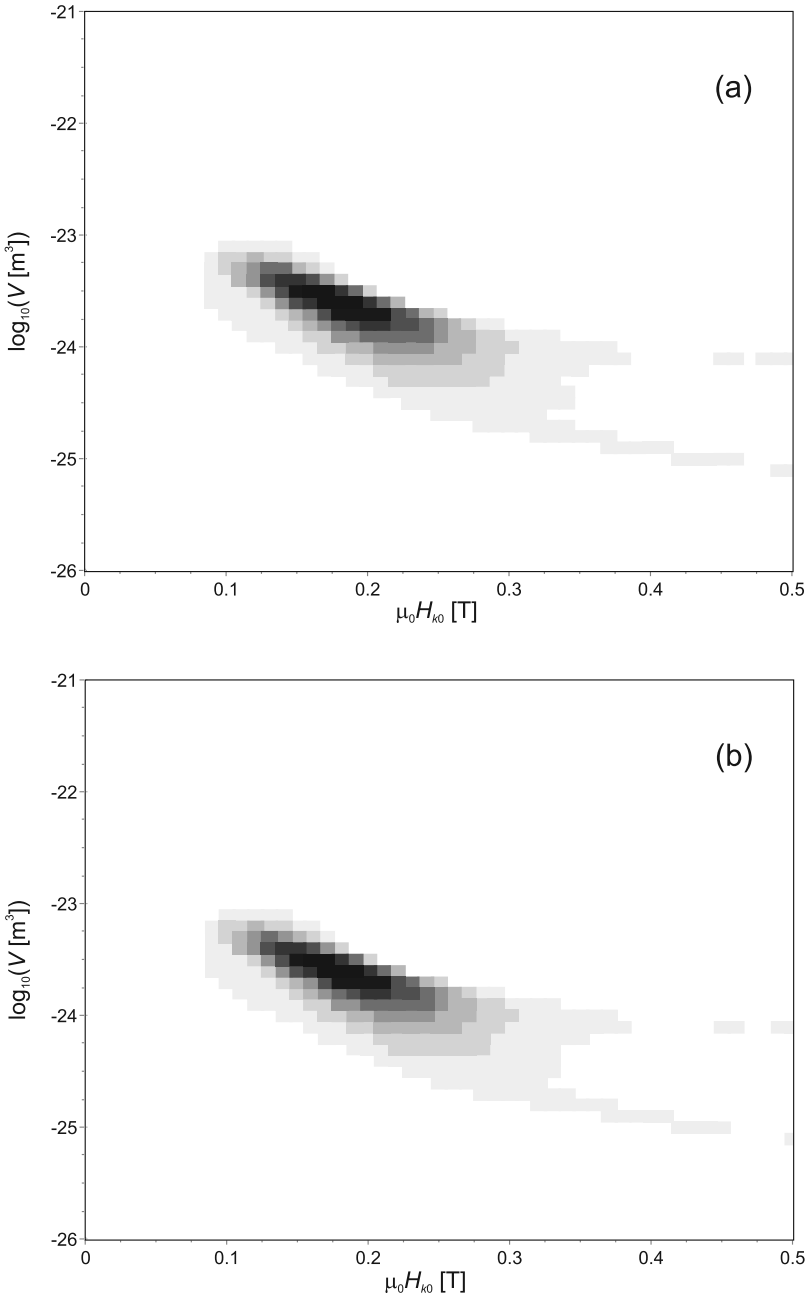

Figure 14. Grain distributions for TC04-12-04 (contour interval = $f_{max}/10$) obtained from two different starting models: (a), a uniform model with ${}^0f(V, H_{K0}) = 0$ for all cells; and (b) a Gaussian coercivity and log-Gaussian size distribution with a peak at $(V, \mu_0 H_{K0}) = (1 \times 10^{-22}$ m^3, 225 mT). In both cases the final model has a mode at $(V, \mu_0 H_{K0}) = (3.2 \times 10^{-24}$ m^3, 180 mT) and a mean of $(V, \mu_0 H_{K0}) = (2.3 \times 10^{-24}$ m^3, 208 mT).

w/L = 0.74, in reasonable agreement with those specified by the manufacturer (10 nm, approximately equidimensional). The greater smearing is presumably a consequence of the very fine size and relatively low microcoercivities of these particles, which place them near the resolution limit of our technique (with measurements down to 10 K).

[57] Susceptibility behavior predicted for the ferrofluid based on the calculated $f(V, H_{K0})$ agrees rather poorly with the observed behavior (Figure 24). The measured susceptibilities show much broader peaks, at higher temperatures: In effect they exhibit the sort of behavior that we would expect for a much broader distribution of grain sizes/shapes, with a higher mean product VH_{K0}. We attribute the difference between measured and predicted behavior primarily to the effects of magnetostatic interactions, which are not included in our model.

5. Discussion

[58] For both the Tiva Canyon Tuff samples and the ferrofluid, independent data on particle sizes and shapes

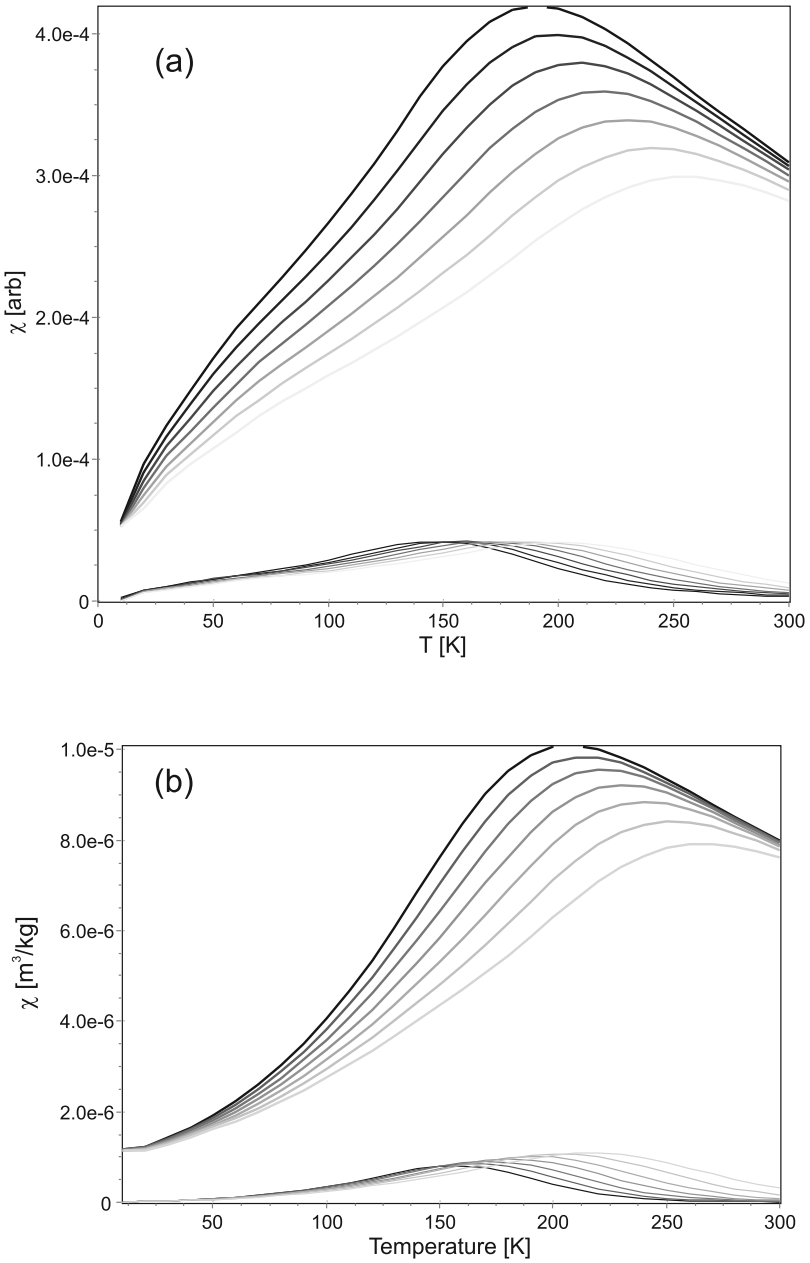

Figure 15. Measured $k(f, T)$ for sample TC04-12-04 (Figure 15b) agrees reasonably well with that calculated from the models of Figure 14 (Figure 15a). Gray scale indicates frequency as in Figure 13.

are available, and thermal fluctuation tomography reconstructs the mean and/or mode of the distribution $f(V, H_{K0})$ quite accurately. Bimodal distributions can be clearly separated, particularly when the product VH_{K0} differs significantly for the different modal dimensions. However it is less clear exactly how much significance can be attached to the finer-scale features of the calculated distributions.

[59] There are two major limiting factors: (1) the restricted range of "viewing angles" available for input to the tomographic algorithm, a limitation imposed by the physics of magnetic blocking; and (2) the string of critical assumptions involved, including: uniform magnetization of the grains; coherent reversal [*Newell and Merrill*, 1999]; angular dependence of switching field $H_{SW}(\varphi)$ according to Stoner-Wohlfarth theory [*Stoner and Wohlfarth*, 1948; see also *Stephenson and Shao*, 1994; *Dunlop and Özdemir*, 1997; *Madsen*, 2002]; dominant shape anisotropy, so that $H_K(T)$ is proportional to $M_S(T)$; lack of magnetostatic interactions; and the grain size and temperature dependence of the thermal fluctuation field as developed from Néel theory by *Egli and Lowrie* [2002].

[60] Let us first consider the general validity of the model and its assumptions. Although our approach was necessitated by instrumental constraints, it has the addi-

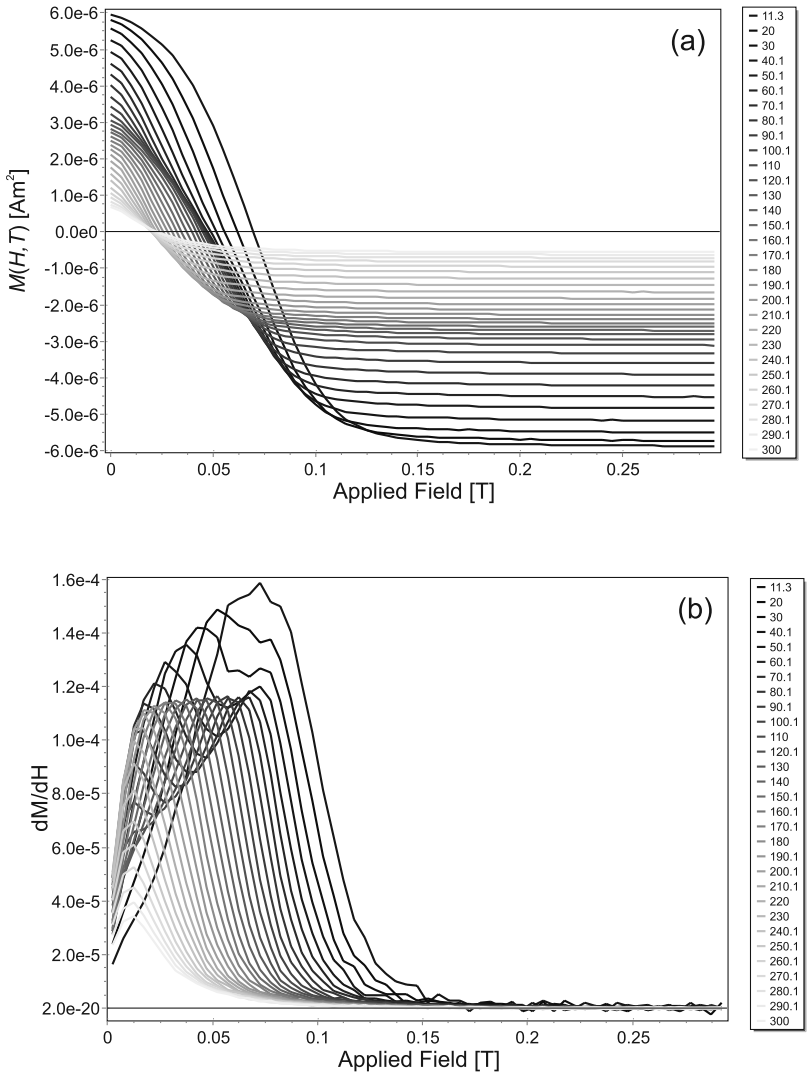

Figure 16. Low-T behavior of a composite sample containing a mixture of two stratigraphic levels in the Tiva Canyon Tuff: Remanent magnetization as a function of (a) applied DC backfield and (b) derivative curves, for temperatures from 10 K to 300 K (ΔT = 10), measured in steps of 5 mT.

tional advantage of providing an overdetermined (or mixed determined) set of equations for determining $f(V, H_{K0})$ and thus it allows evaluation of internal self-consistency of the model and data through goodness-of-fit statistics. In *Dunlop*'s [1965] original method each ΔM measurement uniquely determines $f(V, H_{K0})$ for one small area of the plot (since the pTRMs involve nonoverlapping bands on the Néel plot, and these are chopped into nonoverlapping quadrilaterals by AF demagnetization). In effect the model parameter space is discretized by quadrilateral tiling rather than by rectilinear gridding. The matrix a in equation (13) is in this case a square identity matrix, and each predicted ΔM depends on the value of f for only one cell.

[61] In our approach the integration areas are strongly overlapping (Figure 10), and each predicted ΔM depends on a linear combination of f values for numerous cells. The generally good fits we have obtained for the samples in this study (normalized RMS misfits generally less than 10%) would not be possible unless the assumptions were reasonably fulfilled. We have deliberately focused on samples known to contain dominantly SP/SSD grains, with compositions other than pure magnetite. For pure magnetite, the microcoercivity changes abruptly at the Verwey transition ($T_V \sim 120$ K), and even for elongate SD grains the assumption of dominant shape anisotropy is not valid below T_V because of the strong magnetocrystalline anisotropy of the monoclinic phase [e.g., *Carter-Stiglitz et al.*, 2002]. Slight titanium substitution in the Tiva Canyon samples, and oxidation in the paleosol and ferrofluid, suppress the transition and allow us to use the entire 10–300 K temperature range. For MD grains there is no reason to expect the behavior to obey equations (4)–(8), and although we have not yet run the experiment on such a sample, we expect that the proportional misfit would be much higher than 10%. Single-domain grains larger than a threshold size near 50–70 nm are likely to reverse incoherently [*Newell and Merrill*, 1999], and may

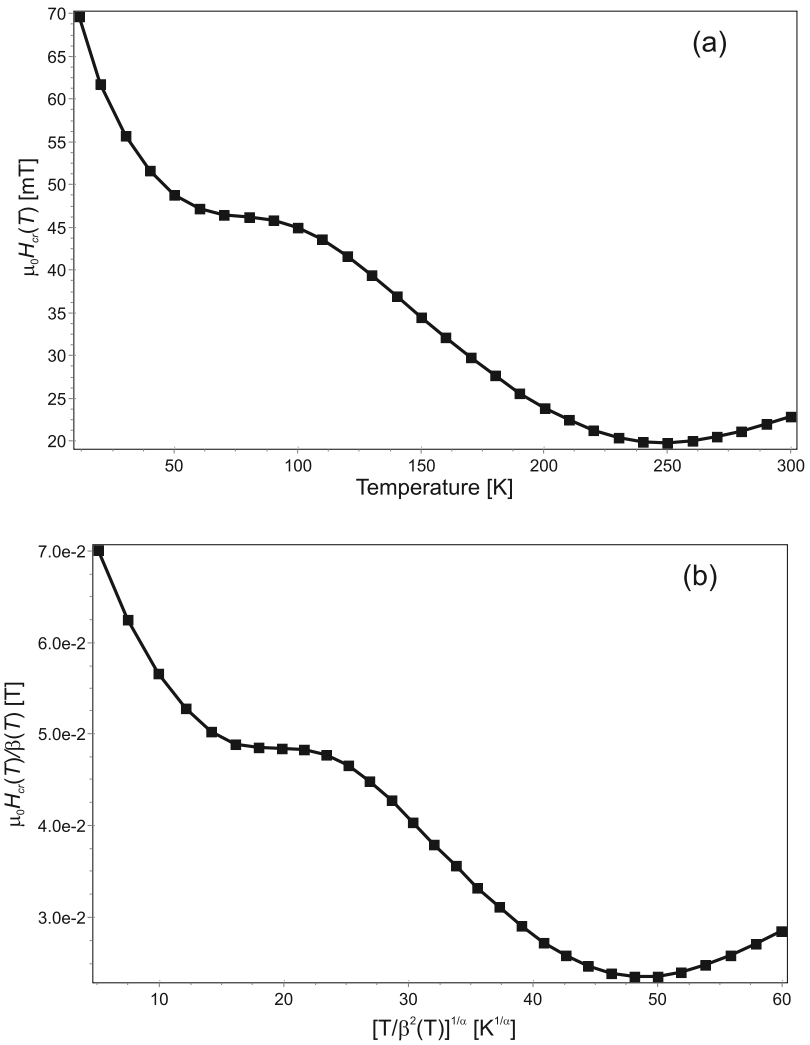

Figure 17. (a) $H_{CR}(T)$ for the composite sample, determined from the data of Figure 16a, is strongly nonlinear. (b) Thermal fluctuation analysis for the mixture using equation (10) yields erroneously large volumes and low coercivities: 1.03×10^{-23} m^3 and 121.89 mT.

also produce artifacts and/or large fitting errors in the reconstructed grain distributions.

[62] Even in the ideal case, however, where particles behave precisely according to theory, there remain resolution limitations in the inversion due to the restricted orientation distribution of integration paths. Some regions of the parameter space are entirely unconstrained by data (Figure 10) in our temperature range ($\geq$10 K) and are therefore completely unresolvable. Areas of marginal resolution are sparsely sampled by subparallel contours, such as the small-V high-H_{K0} region that is stable only at the lowest temperature (Figure 10). Here we cannot resolve variations in $f(V, H_{K0})$ along the nonintersecting contours, exactly equivalent to the nonuniqueness in inverting low-field $\kappa(f, T)$ data [*Shcherbakov and Fabian*, 2005], which represent integrals along nonintersecting hyperbolas. Reasonable resolution can only be expected in the densely sampled region of Figure 10.

[63] All of our models appear to show that V and H_{K0} are distributed not independently but in a covariant way, so that the contours are elongated, more or less along the direction of hyperbolas of constant product VH_{K0}. Such distributions were also obtained by *Dunlop* [1965] [see also *Dunlop and Özdemir*, 1997, sections 8.12 and 17.2.3], for synthetic materials and for lunar samples, so they cannot be entirely dismissed as artifacts specific to our tomographic inversion method. Nevertheless it seems probable that these elongate distributions are artifacts of both inversion methods, through their shared dependence on a physical model and set of assumptions. In particular it appears that the grain orientation distribution, which is treated incompletely in both our calculations and those of *Dunlop* [1965], may be responsible for most of the observed "smearing." As Figure 2 clearly shows, our simplified forward calculations underestimate the width of the coercivity distribution. In the limit of identical particles at zero Kelvin, our model predicts a delta function switching distribution (all grains switching at $H_{app} = 0.524H_{k0}$), whereas a more exact forward calculation would yield a distribution of switching fields

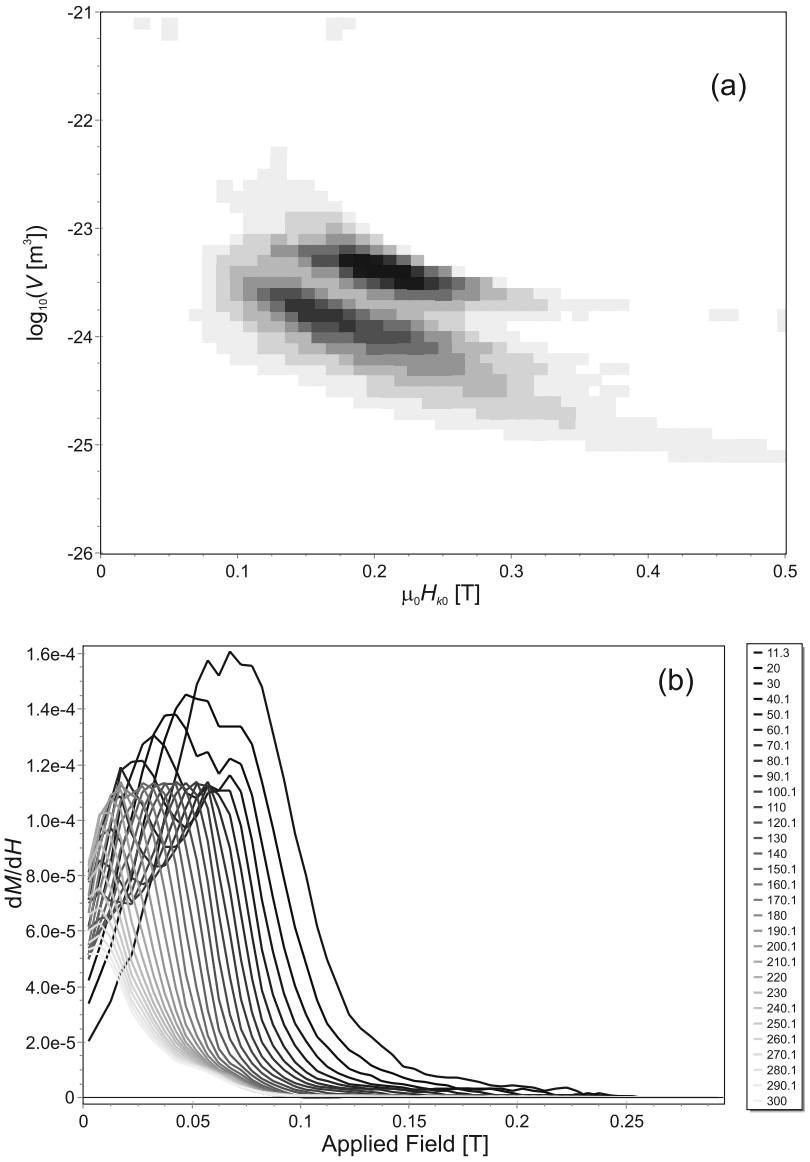

Figure 18. (a) Calculated grain distribution for the mixture of two Tiva Canyon Tuff samples with different mean grain sizes and aspect ratios (contour interval = $f_{max}/10$). (b) Calculated back-field spectra.

with $0.5H_{k0} \leq H_{SW} \leq H_{k0}$. In order to match the broader observed backfield spectra, the inversion is forced to broaden the distribution of microcoercivities, and to introduce a spurious compensating variation in grain volumes. We are currently working on a more accurate forward computation algorithm that is still efficient enough to run iteratively (i.e., one that solves the forward problem by matrix multiplication as in equation (13)).

[64] Linear thermal fluctuation analysis (equations (9) and (10)) is a much faster, simpler way to process the data, but it is also much less effective. Since it uses only one scalar quantity (H_{CR}) derived from the backfield curve for each temperature, the vast majority of the information is discarded, and at best we obtain an estimate of the mean or mode of the distribution. In our calculations for these samples, the results tend to overestimate volumes and to underestimate microcoercivities. Nevertheless they provide reasonable approximations, as long as the distributions are not too broad or polymodal.

[65] The differences between calculated and observed susceptibility behavior are systematically related to the degree of interparticle interaction in the different sample sets. The Tiva Canyon samples show a slight but significant mismatch, with observed susceptibility peaks occurring at slightly higher temperatures than those predicted for the $f(V, H_{K0})$ models. *Worm and Jackson* [1999] showed that according to the strong field remanence tests of *Henkel* [1964] and *Cisowski* [1981], these samples contain almost perfectly noninteracting SD populations. Weak field properties such as κ and ARM are more sensitive to interaction fields, and evidence of weak but nonzero mean fields in the Tiva Canyon samples has been

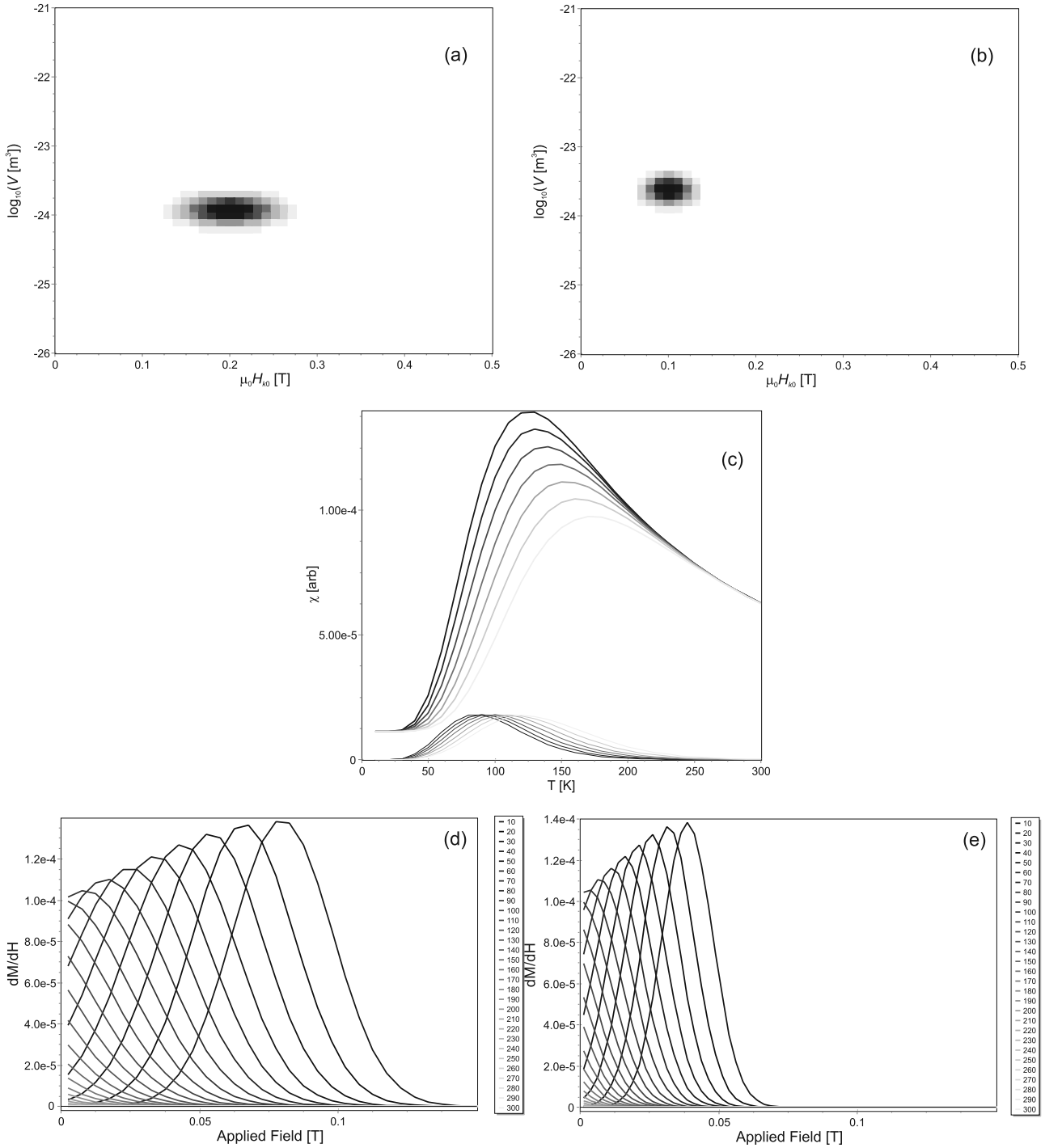

Figure 19. (a) A model with a Gaussian distribution of H_{k0} and log-Gaussian distribution of volumes ($V_{mean} = 1.2 \times 10^{-24}$ m^3, SD = 0.2 log units, $\mu_0 H_{K0mean} = 200$ mT SD = 50 mT) yields (c) the predicted susceptibility behavior. (b) A similar model with twice the mean volume (2.4×10^{-24}) and half the coercivity (100 mT) and the same proportional variances yields exactly the same predicted susceptibility behavior. (d and e) In contrast, the predicted backfield remanence spectra are quite different.

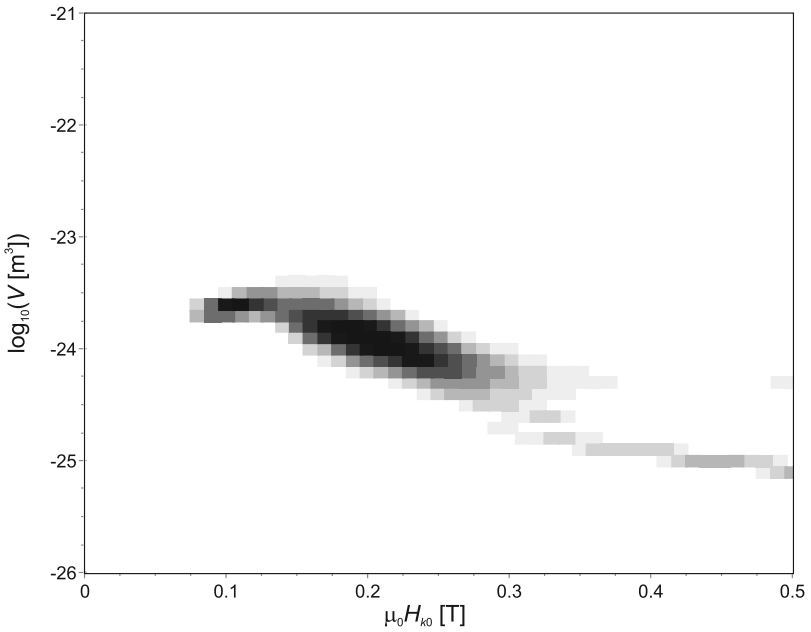

Figure 20. Reconstructed grain distribution for the data set of Figure 19d, using the distribution of Figure 19b as a starting model (contour interval of $f_{max}/10$).

found by *Shcherbakov and Fabian* [2005] and by *Egli and Lowrie* [2002]. The disparity between calculated and observed susceptibility characteristics is larger for the paleosol sample, and largest for the ferrofluid, where interactions may be expected to be quite strong.

[66] *Dunlop*'s [1965] method for determining $f(V, H_{K0})$ has not been widely applied, primarily because of the rarity of natural samples dominated by SSD ferrimagnets. Because of the broader SSD range for harder minerals like hematite and pyrrhotite the technique may be quite usefully adapted by taking $H_K(T) \propto [M_S(T)]^n$, where n depends on the dominant anisotropy [e.g., *Dunlop et al.*, 2000]. Moreover, due to the importance of nanophase ferrimagnets in environmental magnetism, it is of interest to characterize the complete SD (SSD and SP) population, and our extension of *Dunlop*'s [1965] method allows this.

[67] A drawback of our method is the time and expense involved in data collection. To measure 60 back-field remanence steps for each of 30 temperatures takes 4–6 hours and expends ~20 L of liquid helium, using our instrument. We are currently working on adapting our approach to use hysteresis measurements, which require a small fraction of the time. The vertical separation of ascending and descending branches as a function of applied field, called the "delta-M" curve by *Tauxe et al.* [1996], provides an estimate of the switching field distribution [*Jackson et al.*, 1990].

6. Conclusions

[68] Thermomagnetic granulometry methods based on weak field or zero-field properties (e.g., $\kappa(f, T)$ [*Shcherbakov and Fabian*, 2005] and thermal demagnetization spectra [*Worm et al.*, 1988; *Worm and Jackson*, 1999]) require assumptions about $f(H_{k0})$ in order to estimate $f(V)$. *Dunlop*'s [1965] approach for determining the joint distribution $f(V, H_{k0})$ for SSD ensembles, taking advantage of the joint temperature and field dependence of relaxation time, is elegant but not directly adaptable to the study of ultrafine particles that are SP at room temperature. We have developed and tested a new procedure that follows Dunlop's general strategy to obtain $f(V, H_{k0})$ for ensembles containing both SP and SSD grains.

[69] Our iterative algebraic technique uses tomographic reconstruction methods to calculate $f(V, H_{k0})$ from backfield remanence curves measured over a range of temperatures. Previous work has shown that samples from the base of the Tiva Canyon Tuff have narrow size distributions of elongate Ti-poor titanomagnetite [*Schlinger et al.*, 1988, 1991]. Tomographic inversion of the low-temperature backfield spectra yield sharply peaked distributions, from which we calculate modal grain dimensions in excellent agreement with those observed in previous studies. Calculated $\kappa(f, T)$ based on the reconstructed $f(V, H_{k0})$ distributions generally reproduce the observed behavior with good accuracy; slight differences are attributed to weak magnetostatic interactions that affect $\kappa(f, T)$ more significantly than the backfield remanence curves. Inversion of ferrofluid backfield data also yields a $f(V, H_{k0})$ distribution in good agreement with independent characterization. The disagreement between modeled and measured $\kappa(f, T)$ for the ferrofluid is much more substantial, due to the strong interactions.

[70] The central tendency (mean and/or mode) of the $f(V, H_{k0})$ distribution is accurately recovered by the inversion, but finer details have to be interpreted judiciously because of smearing and other artifacts that may be present due to (1) imperfect "ray path" coverage, (2) incomplete account of the grain orientation distribution,

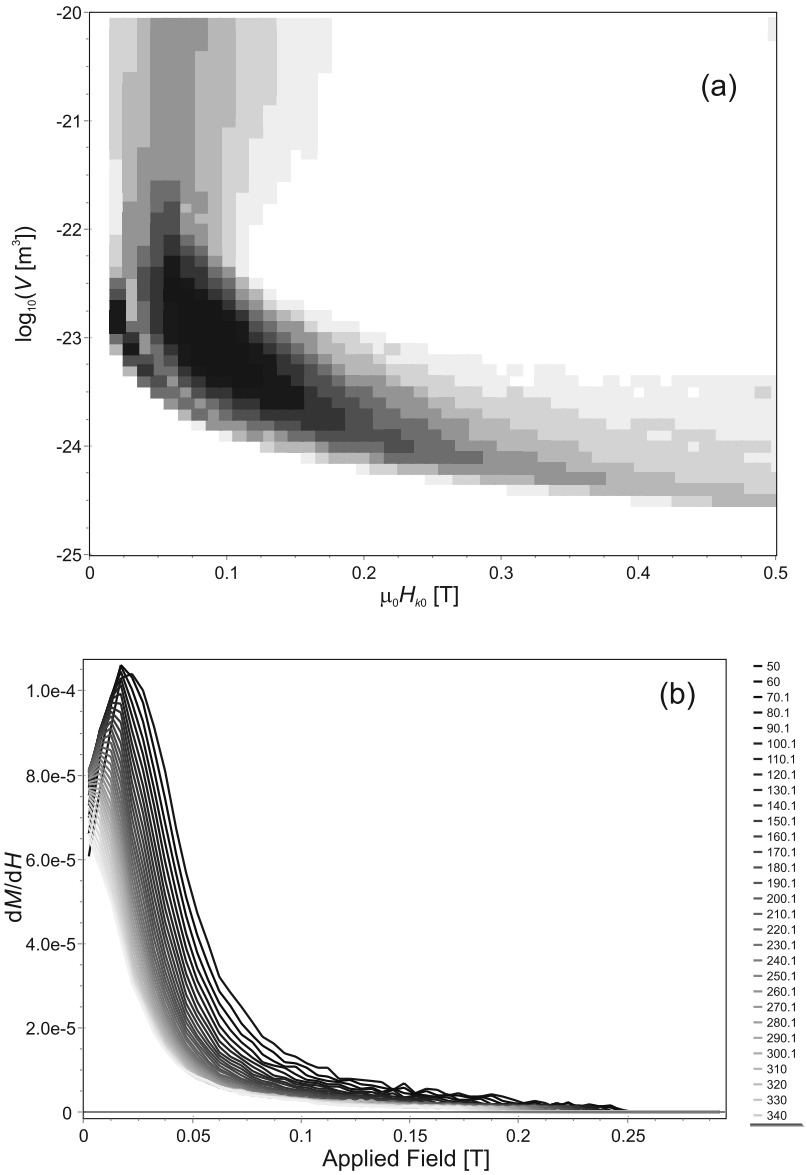

Figure 21. (a) Reconstructed grain distribution (contour interval of $f_{max}/10$) and (b) best fit back-field spectra for the paleosol sample. The RMS misfit is <5%. Note that the V scale in Figure 21a is different than in the other Néel plots in this paper.

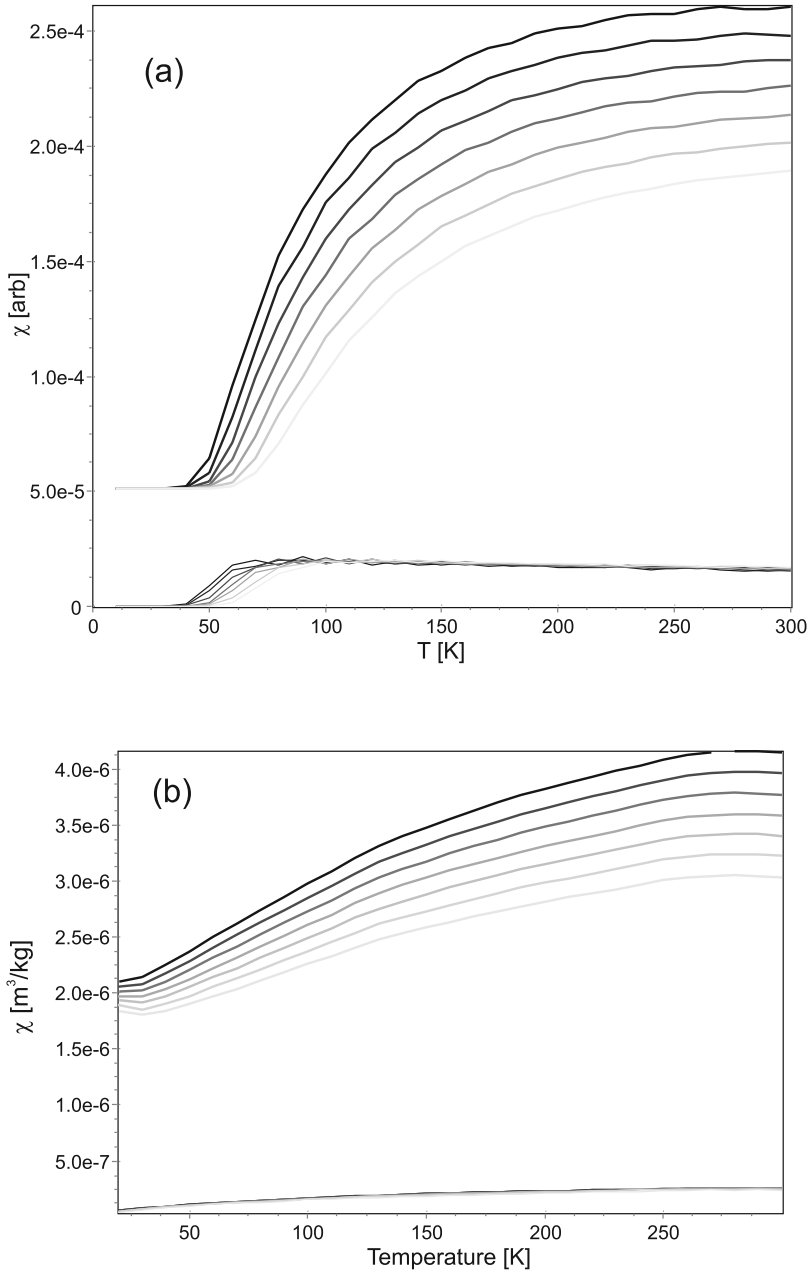

Figure 22. (a) Calculated and (b) measured susceptibilities (in-phase and quadrature) for the paleosol. Frequencies are indicated by gray scale as in Figure 13.

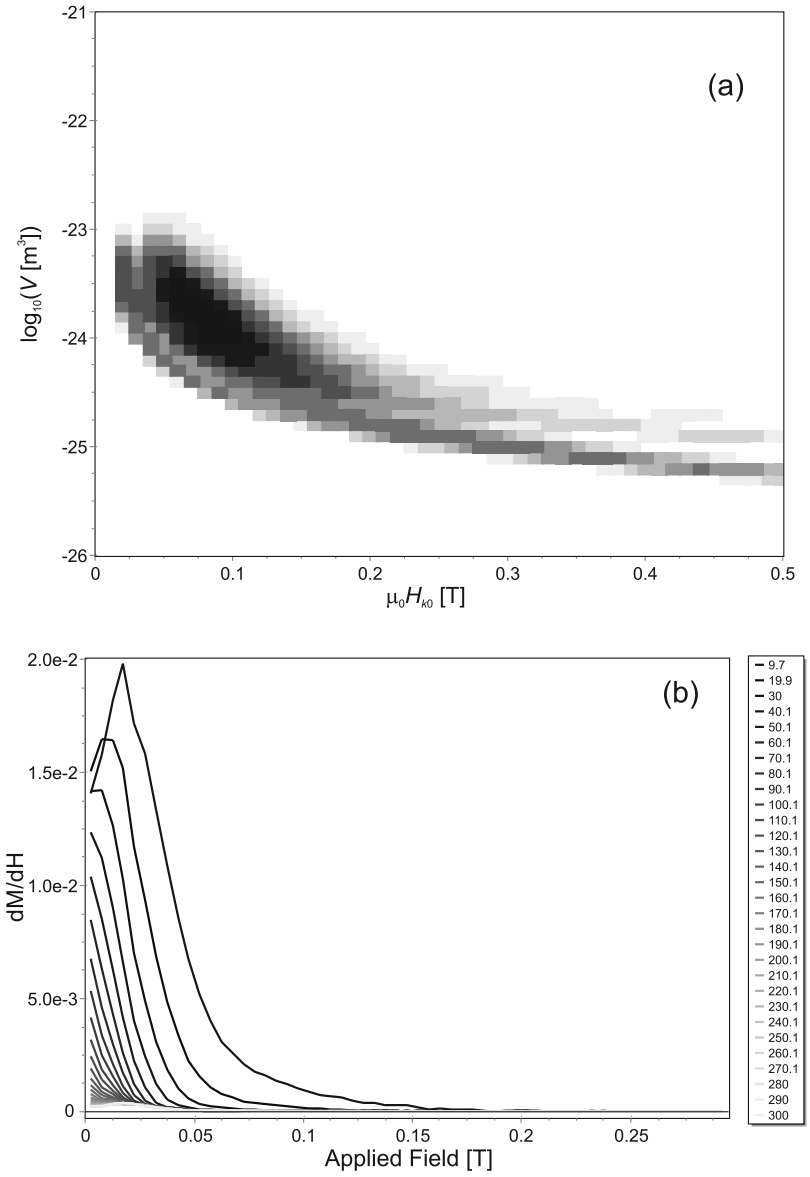

Figure 23. (a) Reconstructed grain distribution (contour interval of $f_{max}/10$) and (b) best fit backfield spectra for the ferrofluid sample. RMS misfit is 9.3%. The distribution mode is at $V = 1.58 \times 10^{-24}$, $\mu_0 H_{K0} = 70$ mT, corresponding to a grain length of 14.2 nm, and aspect ratio of $w/L = 0.74$.

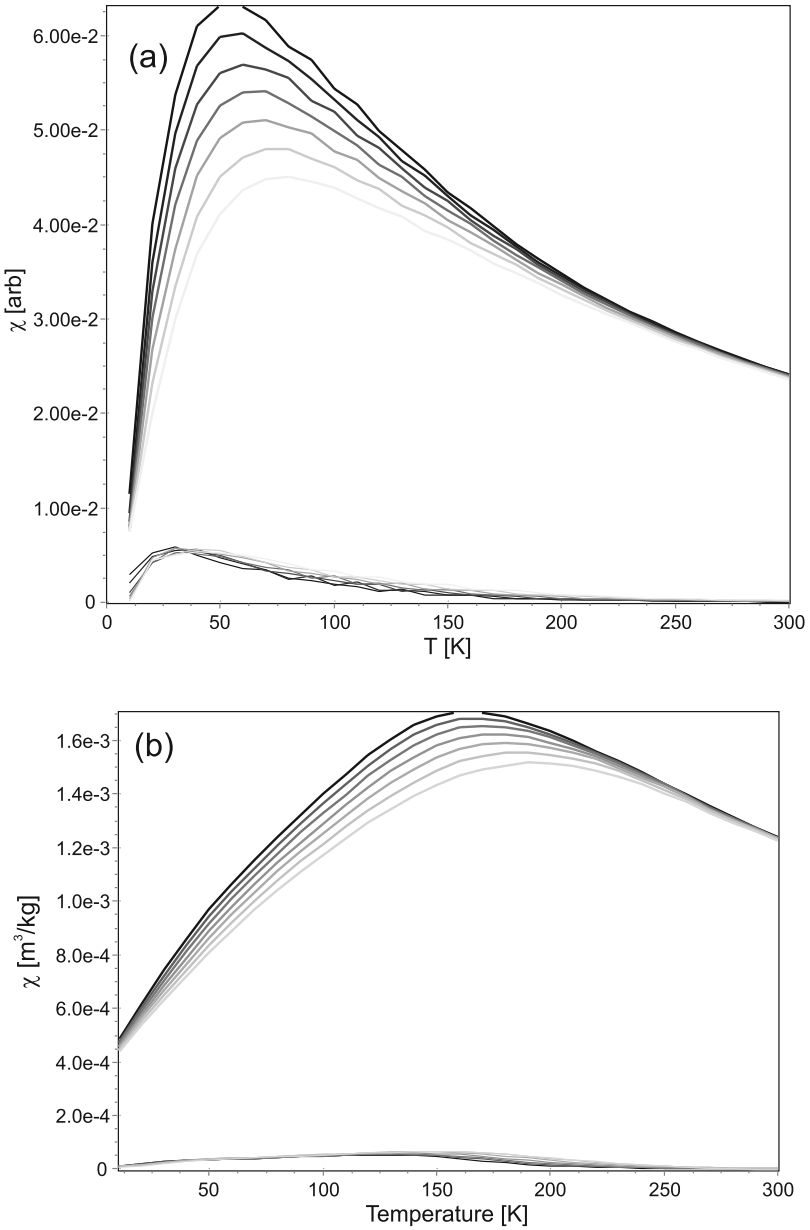

Figure 24. (b) Measured $k(f, T)$ for the ferrofluid sample which agrees poorly with that (a) calculated from the model of Figure 23a.

and (3) possible deviations from numerous model assumptions.

[71] **Acknowledgments.** Many thanks to Joe Rosenbaum for outfitting and guiding our 2004 Yucca Mountain sampling expedition and for specimens and data from his previous sample collections there. Thanks also to Devendra Lal and Jeff Gee for providing the Weinan paleosol sample. We greatly appreciate the thoughtful and constructive review of Karl Fabian. Above all, thanks to David J. Dunlop for inspiring us to study this problem. This work was supported by grants 0218384 and 0317922 from the Instruments and Facilities Program and grant 0309291 from the Geophysics Program of the Earth Science Division of the National Science Foundation. This is IRM publication 0603.

References

Brown, W. F. (1959), Relaxation behavior of fine particles, *J. Appl. Phys.*, *30*, 1305–1325.

Brown, W. F. (1963), Thermal fluctuations of a single-domain particle, *Phys. Rev.*, *130*(5), 1677–1686.

Butler, R. F., and S. K. Banerjee (1975), Theoretical single-domain grain size range in magnetite and titanomagnetite, *J. Geophys. Res.*, *80*, 4049–4058.

Carlut, J., and D. V. Kent (2002), Grain-size-dependent paleointensity results from very recent mid-oceanic ridge basalts, *J. Geophys. Res.*, *107*(B3), 2049, doi:10.1029/2001JB000439.

Carter-Stiglitz, B., M. Jackson, and B. Moskowitz (2002), Low-temperature remanence in stable single domain magnetite, *Geophys. Res. Lett.*, *29*(7), 1129, doi:10.1029/2001GL014197.

Carvallo, C., A. Roberts, R. Leonhardt, C. Laj, C. Kissel, M. Perrin, and P. Camps (2005), Selecting samples for paleointensity measurements with FORC diagrams, *Eos Trans. AGU*, *86*(52), Fall Meet. Suppl., Abstract GP11B-06.

Cisowski, S. (1981), Interacting vs. non-interacting single-domain behavior in natural and synthetic samples, *Phys. Earth Planet. Inter.*, *26*, 77–83.

Coe, R. S., J. Riisager, G. Plenier, R. Leonhardt, and D. Krasa (2004), Multidomain behavior during Thellier paleointensity experiments: Results from the 1915 Mt. Lassen flow, *Phys. Earth Planet. Inter.*, *147*(2–3), 141–153.

Dekkers, M. J. (1997), Environmental magnetism: An introduction, *Geol. Mijnbouw*, *76*, 163–182.

Dormann, J. L., D. Fiorani, and E. Tronc (1997), Magnetic relaxation in fine-particle systems, *Adv. Chem. Phys.*, *98*, 283–494.

Dunlop, D. J. (1965), Grain distributions in rocks containing single-domain grains, *J. Geomagn. Geoelectr.*, *17*, 459–471.

Dunlop, D. J. (1972), Magnetic mineralogy of unheated and heated red sediments by coercivity spectrum analysis, *Geophys. J. R. Astron. Soc.*, *27*, 37–55.

Dunlop, D. J. (1976), Thermal fluctuation analysis: A new technique in rock magnetism, *J. Geophys. Res.*, *81*, 3511–3517.

Dunlop, D. J. (1986), Coercive forces and coercivity spectra of submicron magnetites, *Earth Planet. Sci. Lett.*, *78*, 288–295.

Dunlop, D. J. (2002), Theory and application of the Day plot (M_{rs}/M_s versus H_{cr}/H_c): 2. Application to data for rocks, sediments, and soils, *J. Geophys. Res.*, *107*(B3), 2057, doi:10.1029/2001JB000487.

Dunlop, D. J., and Ö. Özdemir (1997), *Rock Magnetism: Fundamentals and Frontiers*, 573 pp., Cambridge Univ. Press, New York.

Dunlop, D. J., and Ö. Özdemir (2000), Effect of grain size and domain state on thermal demagnetization tails, *Geophys. Res. Lett.*, *27*(9), 1311–1314.

Dunlop, D. J., and G. West (1969), An experimental evaluation of single-domain theories, *Rev. Geophys.*, *7*, 709–757.

Dunlop, D. J., Ö. Özdemir, and P. W. Schmidt (1997a), Paleomagnetism and paleothermometry of the Sydney Basin: 2. Origin of anomalously high unblocking temperatures, *J. Geophys. Res.*, *102*, 27,285–27,295.

Dunlop, D. J., P. W. Schmidt, Ö. Özdemir, and D. A. Clark (1997b), Paleomagnetism and paleothermometry of the Sydney Basin: 1. Thermoviscous and chemical overprinting of the Milton Monzonite, *J. Geophys. Res.*, *102*(B12), 27,271–27,283.

Dunlop, D. J., Ö. Özdemir, D. A. Clark, and P. W. Schmidt (2000), Time-temperature relations for the remagnetization of pyrrhotite (Fe7S8) and their use in estimating paleotemperatures, *Earth Planet. Sci. Lett.*, *176*(1), 107–116.

Dunlop, D. J., B. Zhang, and Ö. Özdemir (2005), Linear and nonlinear Thellier paleointensity behavior of natural minerals, *J. Geophys. Res.*, *110*, B01103, doi:10.1029/2004JB003095.

Egli, R. (2003), Analysis of the field dependence of remanent magnetization curves, *J. Geophys. Res.*, *108*(B2), 2081, doi:10.1029/2002JB002023.

Egli, R. (2004a), Characterization of individual rock magnetic components by analysis of remanence curves. 2. Fundamental properties of coercivity distributions, *Phys. Chem. Earth*, *29*(13–14), 851–867.

Egli, R. (2004b), Characterization of individual rock magnetic components by analysis of remanence curves. 3. Bacterial magnetite and natural processes in lakes, *Phys. Chem. Earth*, *29*(13–14), 869–884.

Egli, R., and W. Lowrie (2002), Anhysteretic remanent magnetization of fine magnetic particles, *J. Geophys. Res.*, *107*(B10), 2209, doi:10.1029/2001JB000671.

Fabian, K. (2001), A theoretical treatment of paleointensity determination experiments on rocks containing pseudo-single or multi domain magnetic particles, *Earth Planet. Sci. Lett.*, *188*(1), 45–58.

Fabian, K. (2006), Approach to saturation analysis of hysteresis measurements in rock magnetism and evidence for stress dominated magnetic anisotropy in young mid-ocean ridge basalt, *Phys. Earth Planet. Inter.*, *154*, 299–307.

Heller, F., and M. E. Evans (1995), Loess magnetism, *Rev. Geophys.*, *33*(2), 211–240.

Heller, F., C.-D. Shen, J. Beer, X.-M. Liu, T.-S. Liu, A. Bronger, M. Suter, and G. Bonani (1993), Quantitative estimates of pedogenic ferromagnetic mineral formation in Chinese loess and palaeoclimatic implications, *Earth Planet. Sci. Lett.*, *114*, 385–390.

Henkel, O. (1964), Remanenzverhalten und Wechselwirkungen in hartmagnetischen Teilchenkollektiven, *Phys. Status Solidi*, *7*, 919–924.

Heslop, D., M. J. Dekkers, P. P. Kruiver, and I. H. M. van Oorschot (2002), Analysis of isothermal remanent magnetization acquisition curves using the expectation-maximization algorithm, *Geophys. J. Int.*, *148*, 58–64.

Hunt, C. P., B. M. Moskowitz, and S. K. Banerjee (1995), Magnetic properties of rocks and minerals, in *Rock Physics and Phase Relations: A Handbook of Physical Constants*, *AGU Ref. Shelf*, vol. 3, edited by T. J. Ahrens, pp. 189–204, AGU, Washington, D. C.

Jackson, M. J., H.-U. Worm, and S. K. Banerjee (1990), Fourier analysis of digital hysteresis data: Rock magnetic applications, *Phys. Earth Planet. Inter.*, *65*, 78–87.

Kak, A. C., and M. Slaney (1988), *Principles of Computerized Tomographic Imaging*, 329 pp., IEEE Press, Piscataway, N. J.

Lanci, L., and D. V. Kent (2003), Introduction of thermal activation in forward modeling of hysteresis loops for single-domain magnetic particles and implications for the interpretation of the Day diagram, *J. Geophys. Res.*, *108*(B3), 2142, doi:10.1029/2001JB000944.

Madsen, K. N. (2002), Angular dependence of switching field measured on maghemite, *J. Magn. Magn. Mater.*, *241*(2–3), 220–227.

Maher, B. A., and R. Thompson (1995), Paleorainfall reconstructions from pedogenic magnetic susceptibility variations in the Chinese loess and Paleosols, *Quat. Res.*, *44*(3), 383–391.

Maher, B. A., and R. Thompson (1999), *Quaternary Climates, Environments and Magnetism*, 390 pp., Cambridge Univ. Press, New York.

Maher, B. A., R. Thompson, and L.-P. Zhou (1994), Spatial and temporal reconstructions of changes in the Asian palaeomonsoon: A new mineral magnetic approach, *Earth Planet. Sci. Lett.*, *125*, 462–471.

Menke, W. (1984), *Geophysical Data Analysis: Discrete Inverse Theory*, 260 pp., Elsevier, New York.

Néel, L. (1949), Théorie du traînage magnétique des ferromagnétiques en grains fins avec applications aux terres cuites, *Ann. Geophys.*, *5*, 99–136.

Newell, A. J. (2005), A high-precision model of first-order reversal curve (FORC) functions for single-domain ferromagnets with uniaxial anisotropy, *Geochem. Geophys. Geosyst.*, *6*, Q05010, doi:10.1029/2004GC000877.

Newell, A. J., and R. T. Merrill (1999), Single-domain critical sizes for coercivity and remanence, *J. Geophys. Res.*, *104*, 617–628.

Özdemir, Ö., and S. K. Banerjee (1984), High temperature stability of maghemite (γ-Fe_2O_3), *Geophys. Res. Lett.*, *11*, 161–164.

Perrin, M. (1998), Paleointensity determination, magnetic domain structure, and selection criteria, *J. Geophys. Res.*, *103*, 30,591–30,600.

Pike, C. R., A. P. Roberts, and K. L. Verosub (2001), First-order reversal curve diagrams and thermal relaxation effects in magnetic particles, *Geophys. J. Int.*, *145*, 721–730.

Roberts, A. P., C. R. Pike, and K. L. Verosub (2000), First-order reversal curve diagrams: A new tool for characterizing the magnetic properties of natural samples, *J. Geophys. Res.*, *105*, 28,461–28,475.

Robertson, D. J., and D. E. France (1994), Discrimination of remanence-carrying minerals in mixtures, using isothermal remanent magnetization acquisition curves, *Phys. Earth Planet. Inter.*, *82*, 223–234.

Rosenbaum, J. G. (1993), Magnetic grain-size variations through an ash-flow sheet: Influence on magnetic properties and implications for cooling history, *J. Geophys. Res.*, *98*, 11,715–11,727.

Schlinger, C. M., J. G. Rosenbaum, and D. R. Veblen (1988), Fe-oxide microcrystals in welded tuff from southern Nevada; origin of remanence carriers by precipitation in volcanic glass, *Geology*, *16*(6), 556–559.

Schlinger, C. M., D. R. Veblen, and J. G. Rosenbaum (1991), Magnetism and magnetic mineralogy of ash flow tuffs from Yucca Mountain, Nevada, *J. Geophys. Res.*, *96*, 6035–6052.

Shcherbakov, V. P., and K. Fabian (2005), On the determination of magnetic grain-size distributions of superparamagnetic particle ensembles using the frequency dependence of susceptibility at different temperatures, *Geophys. J. Int.*, *162*, 736–746.

Spakman, W., and G. Nolet (1988), Imaging algorithms, accuracy and resolution in delay-time tomography, in *Mathematical Geophysics: A Survey of Recent Developments in Seismology and Geodynamics*, edited by N. J. Vlaar et al., pp. 155–188, Springer, New York.

Stephenson, A., and J. C. Shao (1994), The angular dependence of the median destructive field of magnetite particles, *Geophys. J. Int.*, *118*, 181–184.

Stoner, E. C. (1945), The demagnetizing factors for ellipsoids, *Philos. Mag.*, *36*, 803–821.

Stoner, E. C., and E. P. Wohlfarth (1948), A mechanism of magnetic hysteresis in heterogeneous alloys, *Philos. Trans. R. Soc. London, Ser. A*, *240*, 599–602.

Tauxe, L., T. A. T. Mullender, and T. Pick (1996), Potbellies, wasp-waists, and superparamagnetism in magnetic hysteresis, *J. Geophys. Res.*, *101*, 571–583.

Thompson, R., and F. Oldfield (1986), *Environmental Magnetism*, 227 pp., Allen and Unwin, London.

Verosub, K. L., and A. P. Roberts (1995), Environmental magnetism: Past, present, and future, *J. Geophys. Res.*, *100*, 2175–2192.

Victora, R. H. (1989), Predicted time dependence of the switching field for magnetic materials, *Phys. Rev. Lett.*, *63*, 457–460.

Walton, D. (1990), Comment on "Predicted time dependence of the switching field for magnetic materials" by R. H. Victora, *Phys. Rev. Lett.*, *65*, 1170.

Worm, H.-U., and M. Jackson (1999), The superparamagnetism of Yucca Mountain Tuff, *J. Geophys. Res.*, *104*, 25,415–25,425.

Worm, H.-U., M. J. Jackson, P. R. Kelso, and S. K. Banerjee (1988), Thermal demagnetization of partial thermoremanent magnetization, *J. Geophys. Res.*, *93*, 12,196–12,204.

Yu, Y., and D. J. Dunlop (2003), On partial thermoremanent magnetization tail checks in Thellier paleointensity determination, *J. Geophys. Res.*, *108*(B11), 2523, doi:10.1029/2003JB002420.

Yu, Y., and L. Tauxe (2005), Testing the IZZI protocol of geomagnetic field intensity determination, *Geochem. Geophys. Geosyst.*, *6*, Q05H17, doi:10.1029/2004GC000840.

B. Carter-Stiglitz, R. Egli, M. Jackson, and P. Solheid, Institute for Rock Magnetism, Department of Geology and Geophysics, University of Minnesota, 291 Shepherd Laboratories, 100 Union St., S.E., Minneapolis, MN 55455-0128, USA. (irm@tc.umn.edu)